Accepted for publication in the ApJ
Preprint typeset using LaTeX style emulateapj v. 5/2/11

arXiv:1210.6207v1 [astro-ph.GA] 23 Oct 2012

GRAVITATIONAL INSTABILITY OF ROTATING, PRESSURE-CONFINED, POLYTROPIC GAS DISKS WITH VERTICAL STRATIFICATION

Jeong-Gyu Kim[1,2], Woong-Tae Kim[1,2], Young Min Seo[2,3], & Seung Soo Hong[2,4]
[1]Center for the Exploration of the Origin of the Universe (CEOU), Astronomy Program, Department of Physics & Astronomy, Seoul National University, Seoul 151-742, Republic of Korea
[2]FPRD, Department of Physics & Astronomy, Seoul National University, Seoul 151-742, Republic of Korea
[3]Department of Astronomy and Steward Observatory, University of Arizona, Tucson, AZ 85721, USA and
[4]National Youth Space Center, Goheung, Jeolanamdo, 548-951, Republic of Korea

Accepted for publication in the ApJ

ABSTRACT

We investigate gravitational instability (GI) of rotating, vertically-stratified, pressure-confined, polytropic gas disks using linear stability analysis as well as analytic approximations. The disks are initially in vertical hydrostatic equilibrium and bounded by a constant external pressure. We find that GI of a pressure-confined disk is in general a mixed mode of the conventional Jeans and distortional instabilities, and is thus an unstable version of acoustic-surface-gravity waves. The Jeans mode dominates in weakly confined disks or disks with rigid boundaries. When the disk has free boundaries and is strongly pressure-confined, on the other hand, the mixed GI is dominated by the distortional mode that is surface-gravity waves driven unstable under own gravity and thus incompressible. We demonstrate that the Jeans mode is gravity-modified acoustic waves rather than inertial waves and that inertial waves are almost unaffected by self-gravity. We derive an analytic expression for the effective sound speed $c_{\rm eff}$ of acoustic-surface-gravity waves. We also find expressions for the gravity reduction factors relative to a razor-thin counterpart, appropriate for the Jeans and distortional modes. The usual razor-thin dispersion relation after correcting for $c_{\rm eff}$ and the reduction factors closely matches the numerical results obtained by solving a full set of linearized equations. The effective sound speed generalizes the Toomre stability parameter of the Jeans mode to allow for the mixed GI of vertically-stratified, pressure-confined disks.

Subject headings: Hydrodynamics — Instabilities — ISM: kinematics and dynamics — stars: formation — waves

1. INTRODUCTION

Gravitational Instability (GI) plays a crucial role in structure formation in various astronomical situations ranging from growth of primordial density fluctuations to star formation in disk galaxies (e.g., Zel'Dovich 1970; McKee & Ostriker 2007). GI in flattened systems is of particular importance in formation of giant clouds in disk galaxies (e.g., Goldreich & Lynden-Bell 1965a; Elmegreen 1987; Kim et al. 2003), gas giant planets in protoplanetary disks (e.g., Boss 1997; Durisen et al. 2007), and bound clumps resulting from fragmentation of shocked layers in star-forming regions (e.g., Elmegreen & Lada 1977; Elmegreen 1998).

While real astrophysical disks are vertically stratified, most analytic studies often neglect the vertical degree of freedom and adopt an isothermal equation of state (EOS) for simplicity. In a rotating, infinitesimally-thin disk with surface density Σ_0 and sound speed c_s, the local dispersion relation for axisymmetric waves with frequency ω and wavenumber k is given by

$$\omega^2 = c_s^2 k^2 - 2\pi G \Sigma_0 k + \kappa_0^2, \qquad (1)$$

where κ_0 is the epicycle frequency and G is the gravitational constant (e.g., Goldreich & Tremaine 1978; Binney & Tremaine 2008). If the disk is not rotating, sound waves with $k < k_{\rm J} = 2\pi G\Sigma_0/c_s^2$ would become gravitationally unstable. The Coriolis force arising from disk rotation stabilizes long-wavelength perturbations, making the disk Jeans-stable if the Toomre stability parameter satisfies

$$Q_T \equiv \frac{c_s \kappa_0}{\pi G \Sigma_0} > Q_{T,c} = 1, \qquad (2)$$

for any k (e.g., Toomre 1964). When $Q_{T,c} < 1$, on the other hand, thermal pressure and rotation are unable to stop the collapse of over-dense regions.

The thin-disk approximation would be valid as long as vertical motions are unimportant and the scale of interest is much longer than the disk scale height. Nevertheless, it has been well known that finite disk thickness makes some quantitative changes to the characteristic wavelengths and critical Q_T values. For instance, Ledoux (1951) showed that waves in self-gravitating, non-rotating, isothermal disks with scale height $H_0 = c_s^2/(\pi G \Sigma_0)$ become unstable if $kH_0 < 1$, which can be compared with the unstable condition $kH_0 < 2$ of the razor-thin counterpart (see also Simon 1965). For rotating disks, Goldreich & Lynden-Bell (1965a) considered the effect of the finite disk thickness and found that the stability condition changes to $Q_{T,c} = 0.676$. This decrease of the critical Q_T value is due to the dilution of self-gravity at the disk midplane in a vertically stratified disk, which can approximately be treated by multiplying the gravity reduction factor $\mathcal{F} = 1/(1 + kH_0)$ to the second term of the right-hand-side of equation (1) (e.g.,

jgkim@astro.snu.ac.kr
wkim@astro.snu.ac.kr
seo3919@email.arizona.edu
sshong@astro.snu.ac.kr

Elmegreen 1987; Kim et al. 2002; Kim & Ostriker 2007).

While the results of GI in isothermal disks are informative, there are several issues of GI that need clarification in more general situations. First of all, there are many classes of gaseous disks that do not have constant temperature in the vertical direction. Examples include optically thick regions of planet-forming protoplanetary disks (e.g., Bell et al. 1997; D'Alessio et al. 1998; Boley et al. 2007) and accretion disks around compact objects (e.g., La Dous 1994; Lubow & Ogilvie 1998). These disks have often been modeled using a polytropic EOS (e.g., Lubow & Ogilvie 1998; Nelson et al. 2000; Mamatsashvili & Rice 2010). While behavior of various waves in polytropic disks have been studied extensively (e.g., Lin et al. 1990; Korycansky & Pringle 1995; Lubow & Ogilvie 1998; Ogilvie & Lubow 1999), GI of such disks has not been explored in detail. Goldreich & Lynden-Bell (1965a) calculated a stability criterion of a uniformly-rotating polytropic disk, but was limited to the case with the adiabatic index $\gamma = 2$. Larson (1985) studied GI of polytropic disks with arbitrary γ by using approximate scaling relations instead of solving perturbation equations accurately. Recently, Mamatsashvili & Rice (2010) considered vertically-stratified polytropic disks and argued that inertial modes rather than acoustic modes become unstable to self-gravitating perturbations. In this work, we shall clarify using both analytic and numerical approaches that it is the acoustic modes rather than the inertial modes that become unstable.

Second, since the sound speed varies with height in polytropic disks, it is questionable what kind of average is the most appropriate for c_s if one wants to use the stability condition (2). Several numerical studies used the vertically-averaged sound speed (Mejía et al. 2005; Boley et al. 2006) or simply midplane value (Rice et al. 2003, 2005) to evaluate stability of protoplanetary disks, but the usage of these has yet to be justified. Mamatsashvili & Rice (2010) attempted to resolve this ambiguity by introducing $Q_M = \Omega^2/(4\pi G\rho_{00})$ as a three-dimensional stability parameter, where Ω is the local orbital angular velocity and ρ_{00} is the midplane density, but the connection between Q_M and Q_T is uncertain since the former does not depend on c_s explicitly. In this work, we define the effective sound speed that well represents the modal behavior of acoustic waves in a thermally stratified disk and show that this naturally relates Q_T to Q_M.

The third issue involves disk truncation by external pressure. Galactic disks are confined by ram pressure of infalling gas (e.g., Dubois & Teyssier 2008) or hot halo gas (e.g., Goldreich & Lynden-Bell 1965a; Lee & Hong 2007). Thin shells produced by supernovae, stellar winds, or expanding H II regions are usually bounded by shocks (e.g., Deharveng et al. 2005; Churchwell et al. 2006, 2007). Elmegreen & Elmegreen (1978) showed that pressure-confined disks become unstable at scales smaller than the Jeans wavelength $\lambda_{\rm J} = c_s^2/(\pi G\Sigma_0)$ of unbounded disks. The mass of fragments produced by such GI is less than the critical Bonnor-Ebert mass, and thus may not necessarily experience gravitational runaway. When the confining pressure is very strong, Lubow & Pringle (1993) showed that the GI becomes essentially the same as that of an incompressible disk, which is in stark contrast to the conventional Jeans instability of compressional disks. Umekawa et al. (1999) and Wünsch et al. (2010) confirmed such predictions by using numerical simulations. Boyd & Whitworth (2005) suggested the GI of strongly confined disks as a potential candidate for forming "free-floating" planetary-mass objects (having mass as low as $\sim 0.003 M_\odot$) detected in young star clusters (e.g., Zapatero Osorio et al. 2002). More elaborate theoretical and numerical models including the effects of shell expansion and deceleration (e.g., Elmegreen 1989; Iwasaki et al. 2011; Dale et al. 2011), thermal and chemical processes (Hosokawa & Inutsuka 2006), boundary conditions (e.g., Elmegreen 1989; Usami et al. 1995; Dale et al. 2009), magnetic fields (Nagai et al. 1998), etc. examined consequences of GI occurring under high external pressure.

Despite these efforts, however, the physical mechanism behind the GI of strongly pressure-confined disks still remains controversial. For example, Lubow & Pringle (1993) argued that the instability is due to a neutral mode that exists because external pressure can hold the layer to any distorted shape, while Elmegreen (1989) and Umekawa et al. (1999) claimed that the distortion of the surfaces exerts a pinching force that causes the distorted disk to collapse. On the other hand, Wünsch et al. (2010) and Dale et al. (2011) considered the collapse of an oblate spheroid with uniform density pressurized by an ambient medium (see also Boyd & Whitworth 2005), and termed the enhanced GI "pressure-assisted gravitational instability", although the physical processes responsible for it were not identified. Very recently, Iwasaki et al. (2011) studied GI of pressure-confined shells around expanding H II regions taking into account boundary effects. They suggested from the vertical behaviors of eigenfunctions that the restoring force of the unstable mode comes from surface-gravity waves. We use both numerical and analytic approaches to confirm that it is indeed surface-gravity waves that become unstable in strongly confined disks.

In this paper, we investigate GI of rotating, vertically-stratified, pressure-confined gas disks. We adopt simple polytropic, rotating models of Goldreich & Lynden-Bell (1965a) and extend them to pressure-confined situations. This work also extends the case of non-rotating, isothermal models of Elmegreen & Elmegreen (1978) to rotating, polytropic disks. Our objectives are four-fold. First, we wish to distinguish conventional Jeans instability from the GI arising from the surface distortion of strongly pressure-confined disks, and give a clear physical explanation for the latter that has previously been confusing. Second, we provide analytic expressions for the effective sound speed $c_{\rm eff}$ that best represents the modal behavior of sound waves in polytropic disks. Third, we find the gravity reduction factors caused by finite disk thickness for the Jeans and distortional modes of GI. We show that the numerical dispersion relations found by solving a full set of perturbation equations are well matched by equation (1) provided that c_s is changed to $c_{\rm eff}$ and that the appropriate reduction factor is considered in the gravity term. Finally, we generalize the Toomre stability parameter of razor-thin disks to vertically-stratified, pressure-bounded disks. While our disk models are simple with a polytropic EOS and without considering external gravity, some qualitative properties of GI clarified in this paper can hold true in more general situations such as disks with a barotropic EOS and/or with external gravity.

The remainder of this paper is organized as follows. In Section 2, we introduce basic equations, construct an equilibrium model, and present linearized perturbation equations. In Section 3, we derive expressions for the effective sound speed $c_{\rm eff}$ that describe the phase speeds of fundamental modes in non-self-gravitating, non-rotating disks. In Section 4, we present the gravity reduction factors $\mathcal{F}$, and show that an approximate dispersion relation using $c_{\rm eff}$ and $\mathcal{F}$ is in excellent agreement with the numerical results obtained by solving the perturbation equations. For rotating disks, we define a stability parameter using $c_{\rm eff}$ that is applicable also to the distortional mode. In Section 5, we summarize and discuss our results.

2. FORMULATIONS

We consider a rotating, self-gravitating, gaseous disk in vertical hydrostatic equilibrium and analyze its stability to small-amplitude, axisymmetric perturbations. The disk is infinitely extended in the horizontal direction, but truncated at a finite height by a tenuous external medium with pressure $p_{\rm ext}$. For local modes in the horizontal direction, it is advantageous to consider a local Cartesian reference frame whose center lies at a radius R_0 and orbits the disk center with a fixed angular velocity $\Omega_0 = \Omega(R_0)$. In this local frame, radial, azimuthal, and vertical coordinates are represented by $x = R - R_0$, $y = R_0(\phi - \Omega_0 t)$, and z, respectively, and the terms arising from curvature effect are ignored (e.g., Goldreich & Lynden-Bell 1965b; Julian & Toomre 1966; Kim et al. 2002). Assuming that the shear rate $q \equiv -d\ln\Omega/d\ln R|_{R_0}$ is uniform, the equilibrium background velocity field is given by $\mathbf{u}_0 = -q\Omega_0 x\mathbf{e}_y$ and the local epicyclic frequency is $\kappa_0^2 = (4-2q)\Omega_0^2$. The equations of ideal hydrodynamics expanded in the local frame are

$$\frac{\partial\rho}{\partial t} + \nabla\cdot(\rho\mathbf{u}) = 0, \tag{3}$$

$$\frac{\partial\mathbf{u}}{\partial t} + \mathbf{u}\cdot\nabla\mathbf{u} = -\frac{1}{\rho}\nabla p - \nabla\psi + 2q\Omega_0^2 x\mathbf{e}_x - 2\mathbf{\Omega}_0\times\mathbf{u}, \tag{4}$$

$$\nabla^2\psi = 4\pi G\rho, \tag{5}$$

where ρ, $\mathbf{u}$, p, and ψ denote mass density, velocity, thermal pressure, and self-gravitational potential of the gas, respectively. To close the set of equations (3)-(5), we assume that the gas follows a polytropic EOS

$$p = K\rho^\gamma, \tag{6}$$

where K is an arbitrary constant and γ is the polytropic exponent. If γ is different from an adiabatic exponent of disturbances, the system under consideration exhibits complicated modal behaviors associated with convective motions. However, Mamatsashvili & Rice (2010) showed that the convective modes do not affect the properties of GI much. In this work, we thus simply take γ equal to the adiabatic exponent.

2.1. *Initial Equilibria*

We first explore equilibrium profiles of density and temperature in purely self-gravitating, polytropic disks confined by an external medium. The pressure confinement model we adopt is a straightforward extension of isothermal disks studied by Elmegreen & Elmegreen (1978) to polytropic cases. For hydrostatic equilibrium in the vertical direction, equations (4) and (5) require

$$\frac{1}{\rho_0}\frac{dp_0}{dz} = -\frac{d\psi_0}{dz}, \tag{7}$$

$$\frac{d^2}{dz^2}\psi_0 = 4\pi G\rho_0, \tag{8}$$

where the subscript "0" denotes the unperturbed state.

Following Elmegreen & Elmegreen (1978), it is convenient to convert the vertical coordinate z to the dimensionless variable μ defined by

$$\mu \equiv \frac{1}{4\pi G\rho_{00}H_0}\frac{d\psi_0}{dz}, \tag{9}$$

where $\rho_{00} = \rho_0(0)$ and H_0 is the disk scale height

$$H_0^2 \equiv \frac{K}{2\pi G\rho_{00}^{2-\gamma}}. \tag{10}$$

In Appendix A, we show that equations (7) and (8) subject to the symmetry condition $d\rho_0/dz = 0$ at $z = 0$ yield the solution

$$\rho_0 = \rho_{00}(1-\mu^2)^{1/\gamma}, \tag{11}$$

(see also Harrison & Lake 1972). The corresponding local speed of sound is

$$c_s^2 = \gamma p_0/\rho_0 = c_{s0}^2(1-\mu^2)^{1-1/\gamma}, \tag{12}$$

where $c_{s0} \equiv (\gamma p_{00}/\rho_{00})^{1/2} = (\gamma K\rho_{00}^{\gamma-1})^{1/2}$ is the midplane sound speed.

Figure 1 plots equilibrium structures of self-gravitating polytropic disks with differing γ. For a softer EOS (smaller γ), mass density falls off more rapidly from the midplane to provide the pressure support against the gravity $\sim 4\pi G\rho_{00}z$ at $|z|/H_0 \lesssim 1$. This in turn makes the gravity smaller at high-altitude regions, causing the density to decrease slower with height at $|z|/H_0 > 1$. As γ increases, therefore, the density becomes more concentrated toward the midplane. For $\gamma > 1$, equation (A9) implies that the density becomes automatically zero at finite height

$$\frac{|z_{\rm cut}|}{H_0} = \frac{\sqrt{\pi}}{2}\frac{\Gamma(1-1/\gamma)}{\Gamma(3/2-1/\gamma)}, \tag{13}$$

where Γ is the Gamma function, indicating that disks with $\gamma > 1$ are truncated even without external pressure. The sound speed in a disk with $\gamma > 1$ decreases monotonically with increasing z. Note that $|z_{\rm cut}| = \infty$ for $\gamma \le 1$.

Now we allow for the truncation of a disk at height $z = \pm a$ due to an external pressure $p_{\rm ext}$. The condition of pressure equilibrium at the boundaries requires

$$A \equiv \mu(z=\pm a) = \left(1 + \frac{2p_{\rm ext}}{\pi G\Sigma_0^2}\right)^{-1/2}, \tag{14}$$

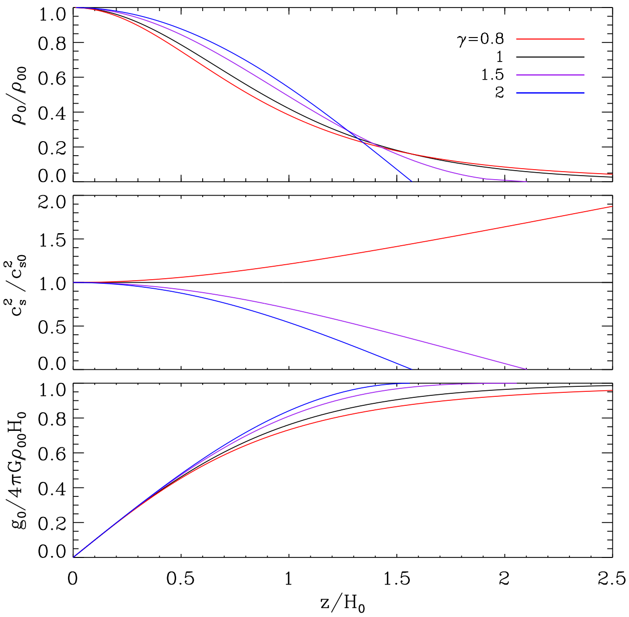

Figure 1. Distributions of density ρ_0 (top), local sound speed c_s (middle), and vertical gravity $g_0 = d\psi_0/dz$ (bottom) in hydrostatic equilibrium of self-gravitating polytropic disks with exponent γ. A stiffer equation of state (larger γ) leads to a flatter density profile near the midplane. Even without external pressure, disks with $\gamma > 1$ are truncated at a finite height (eq. [13]). For $\gamma < 1$, c_s is an increasing function of z.

(e.g., Elmegreen & Elmegreen 1978). Using equation (A8), the column density of the bounded layer is given by

$$\Sigma_0 = \int_{-a}^{+a} \rho_0 \, dz = 2\rho_{00} A H_0 = 2\rho_{00} H \,, \tag{15}$$

where $H \equiv AH_0$ is the effective half-thickness of the layer. The relative density drop at the boundaries is $\rho_{0a}/\rho_{00} = (1 - A^2)^{1/\gamma}$ where $\rho_{0a} = \rho_0(z = a)$. Note that $A = 1$ when $a = |z_{\rm cut}|$, corresponding to no pressure truncation. As $p_{\rm ext}$ increases, the vertical sound crossing time ($\sim H/c_{s0}$) becomes smaller than the internal free-fall time ($\sim (2\pi G\rho_{00})^{-1/2}$). In the limit of $A \to 0$, the disk takes uniform density and $H \to a$ regardless of γ: in this case, self-gravity is so weak that the initial equilibrium is maintained by balance between $p_{\rm ext}$ and p_{00}.

2.2. *Perturbation Equations*

We apply small-amplitude perturbations to the initial equilibrium configurations described above. Equations (3)–(5) are linearized to

$$\frac{\partial \rho_1}{\partial t} + \nabla \cdot (\rho_0 \mathbf{u}_1) = 0 \,, \tag{16}$$

$$\frac{\partial \mathbf{u}_1}{\partial t} = \frac{\rho_1}{\rho_0^2}\nabla p_0 - \frac{1}{\rho_0}\nabla p_1 - \nabla\psi_1 + q\Omega_0 u_{1x}\mathbf{e}_y - 2\mathbf{\Omega}_0 \times \mathbf{u}_1 \,, \tag{17}$$

$$\nabla^2\psi_1 = 4\pi G\rho_1 \,, \tag{18}$$

where the subscript "1" indicates the perturbed quantities.

We further assume that perturbations are axisymmetric and of plane-wave type

$$q_1(x, z, t) = q_1(z)\exp(i\omega t + ik_x x) \,, \tag{19}$$

where q_1 refers to any perturbed variable with frequency ω and radial wavenumber k_x. Then, equations (16)–(18) can be reduced to four first-order ordinary differential equations

$$\frac{d\xi_{1z}}{dz} = \frac{k_x^2}{\omega^2 - \kappa_0^2}(h_1 + \psi_1) - \frac{1}{c_s^2}(h_1 - g_0\xi_{1z}) \,, \tag{20}$$

$$\frac{dh_1}{dz} = \omega^2\xi_{1z} - \psi_1' \,, \tag{21}$$

$$\frac{d\psi_1}{dz} = \psi_1' \,, \tag{22}$$

$$\frac{d\psi_1'}{dz} = k_x^2\psi_1 + \frac{4\pi G\rho_0}{c_s^2}h_1 \,, \tag{23}$$

where ξ_{1z} is the vertical Lagrangian displacement defined through $u_{1z} = \partial\xi_{1z}/\partial t$, $h_1 = p_1/\rho_0$ is the perturbed enthalpy, and $\psi_1' = d\psi_1/dz$. We take ξ_{1z}, h_1, ψ_1, and ψ_1' as four independent variables.

The set of the perturbation equations (20)–(23) are to be integrated numerically along the vertical direction to yield a dispersion relation $\omega = \omega(k_x)$ that satisfies the boundary conditions (BCs) as well as the constraints of even-symmetry modes. To separate the distortional modes of GI from the conventional Jeans modes, we consider two distinct conditions at the boundaries: the rigid boundary that allows only the Jeans modes and the free boundary in which Jeans and distortional modes coexist. Appendix B describes the BCs we adopt. Appendix C presents the numerical method we follow to obtain full dispersion relations, which will be compared with approximate dispersion relations in Sections 3 and 4.

For future purposes, we note that the total perturbed density ρ_1 is a superposition of the perturbed density $\rho_{1,i}$ inside the disk due to wave motions and the perturbed density $\rho_{1,s}$ at $z = \pm a$ due to the surface distortion:

$$\rho_1 = \rho_{1,i} + \rho_{1,s}, \tag{24}$$

where

$$\rho_{1,s} = \rho_{0a}\xi_{1z}\big|_{z=a}\delta(|z| - a), \tag{25}$$

for even-symmetry modes. Here, δ is the Dirac delta function. The corresponding perturbations in the surface density can be written as $\Sigma_1 = \Sigma_{1,i} + \Sigma_{1,s}$. We define

$$w \equiv \frac{\Sigma_{1,i}}{\Sigma_{1,i} + \Sigma_{1,s}}, \tag{26}$$

as the fraction of the perturbed surface density inside the disk relative to the total perturbed surface density. We will show that w defined in equation (26) is a key parameter that controls the relative importance of the Jeans modes to the distortional modes.

2.3. *Classification of Local Modes*

Ignoring waves arising from surface distortion, the perturbation equations (20)–(23) give rise to two principal types of waves: inertial waves and acoustic waves, both modified by self-gravity. The former is characterized by epicycle motions, while the latter is based on gas compressibility. Mamatsashvili & Rice (2010) argued that inertial modes, rather than acoustic modes, are strongly influenced by self-gravity to become unstable. In Appendix D, we classify two types of waves using the local dispersion relations and compare them with the numerical results. We directly demonstrate that while the inertial modes are not much affected by self-gravity and thus remain stable, it is the fundamental acoustic modes that can become unstable in the presence of self-gravity. This makes sense since both acoustic waves and self-gravity rely on density perturbations, while inertial waves are incompressible in nature (e.g., Latter & Balbus 2009).

Before exploring numerical dispersion relations, some physical insight on the fundamental acoustic waves in disks can be gleaned by integrating equation (16) and the horizontal component of equation (17) multiplied by ρ_0 over z. With the help of equation (19), we obtain

$$\omega^2 = k_x^2 \Sigma_0 \frac{\widehat{h}_1 + \widehat{\psi}_1}{\Sigma_1} + \kappa_0^2, \tag{27}$$

where the hat indicates the density-weighted vertical averages (i.e., $\widehat{q}_1 = \int \rho_0 \, q_1 \, dz/\Sigma_0$). Because $\widehat{h}_1$, $\widehat{\psi}_1$, and Σ_1 are interrelated with each other and generally depend on k_x and ω, one needs to solve equations (20)–(23) numerically to obtain full dispersion relations. Nevertheless, equation (27) implies that ω^2 consists of three terms, each responsible for the effect of pressure (including thermal pressure and surface distortion), self-gravity, and the Coriolis force, as in equation (1). This opens a possibility that by finding solutions of $\widehat{h}_1$ and $\widehat{\psi}_1$ independent of ω in some suitable limits, one can obtain an approximate dispersion relation that matches the numerical results closely. We will focus on this in the remainder of this paper.

3. NON-SELF-GRAVITATING FUNDAMENTAL MODES

As mentioned before, the sound speed of polytropic disks varies with the vertical height, so that it is interesting to find an effective sound speed that best represents modal behavior of waves propagating throughout the disk. Also of interest is the effect of surface distortion on sound waves in the case of the free boundaries. To address these issues, we in this section limit ourselves to the fundamental acoustic modes in non-self-gravitating disks. For simplicity, we ignore the effect of disk rotation, which merely adds κ_0^2 to ω^2 (see eq. [27]).

3.1. *Rigid Boundary*

In non-self-gravitating, non-rotating disks, equation (27) is reduced to

$$\omega^2 = \frac{\Sigma_0 \widehat{h}_1}{\Sigma_1} k_x^2 = \frac{\int \rho_0 h_1 dz}{\Sigma_{1,i} + \Sigma_{1,s}} k_x^2 = c_{\rm eff}^2 k_x^2, \tag{28}$$

where $c_{\rm eff}$ is the effective sound speed. When the boundaries are rigid or $A = 1$, $\Sigma_{1,s} = 0$ and

$$c_{\rm eff}^2 \equiv \frac{\int \rho_1 c_s^2 \, dz}{\int \rho_1 \, dz} = \frac{\int_{-a}^{a} \rho_0 h_1 \, dz}{\int_{-a}^{a} \rho_0 h_1 / c_s^2 \, dz}. \tag{29}$$

Equation (29) shows that excited waves are pure acoustic modes (p modes) whose restoring force is the thermal pressure. Obviously, $c_{\rm eff} = c_{s0}$ in an isothermal disk. Note that we did not make any approximation in deriving equations (28) and (29) except for ignoring the effects of self-gravity and rotation.

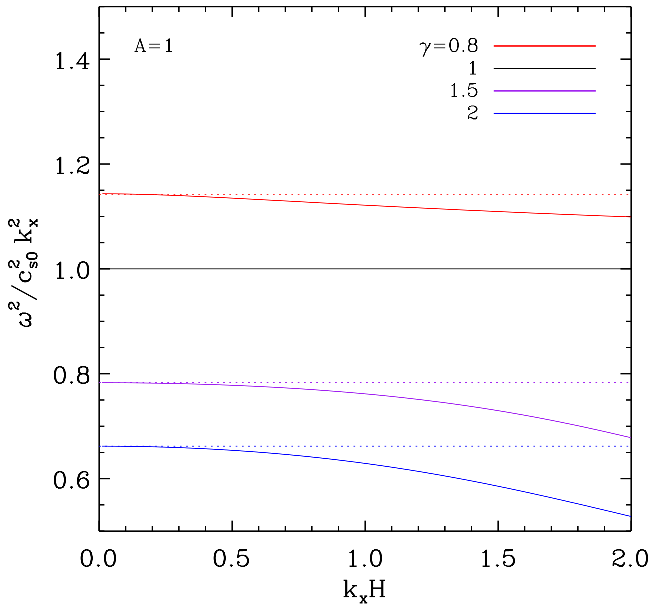

Figure 2. Dispersion relations of the fundamental acoustic modes in non-self-gravitating, non-rotating, vertically-stratified, polytropic disks with $A = 1$ and $\gamma = 0.8, 1, 1.5, 2$. The frequency ω in the ordinate is normalized by $c_{s0} k_x$. Horizontal dotted lines mark $c_{\rm eff}^2/c_{s0}^2$ ($\equiv \alpha$) (eq. [31]) in the long wavelength limit.

Now consider the fundamental mode in the long-wavelength limit. Appendix E shows that the fundamental acoustic waves have a simple solution $h_1(z) =$ constant in the limit of $k_x \to 0$. Equation (29) is then simplified to

$$c_{\rm eff}^2 = \widetilde{c_s}^2 \equiv \frac{\int_{-a}^{a} \rho_0 \, dz}{\int_{-a}^{a} \rho_0 / c_s^2 \, dz}, \quad \text{for rigid BC}, \tag{30}$$

indicating that the effective sound speed corresponds to the density-weighted, harmonic mean of the local sound speeds. For polytropic disks, the ratio of the effective sound speed to the midplane sound speed is given analytically by

$$\alpha \equiv \widetilde{c_s}^2 / c_{s0}^2 = {}_2F_1(\tfrac{1}{2}, 1 - \tfrac{1}{\gamma}; \tfrac{3}{2}; A^2)^{-1}, \tag{31}$$

where ${}_2F_1$ denotes the Gaussian hypergeometric function. Disks with $\gamma > 1$ have $\alpha < 1$ since the temperature decreases monotonically with height. When there is no external confining medium ($A = 1$), α varies smoothly from $3/2$ to $2/\pi$ for $0.5 < \gamma < 2$. Larger external pressure makes α closer to unity.

To check the applicability of equation (30) for waves with finite wavelengths, we obtain numerical dispersion relations of pure acoustic waves in non-self-gravitating, non-rotating disks for $A = 1$ and $\gamma = 0.8$, 1, 1.2, and 2, by following the procedures given in Appendix C. Figure 2 plots the resulting numerical dispersion relations using solid lines, which can be compared with the approximate dispersion relation (28) together with equation (30) shown as dotted lines. When $\gamma = 1$, the dispersion relation is simply $\omega^2 = c_{s0}^2 k_x^2$. When $\gamma \neq 1$, the numer-

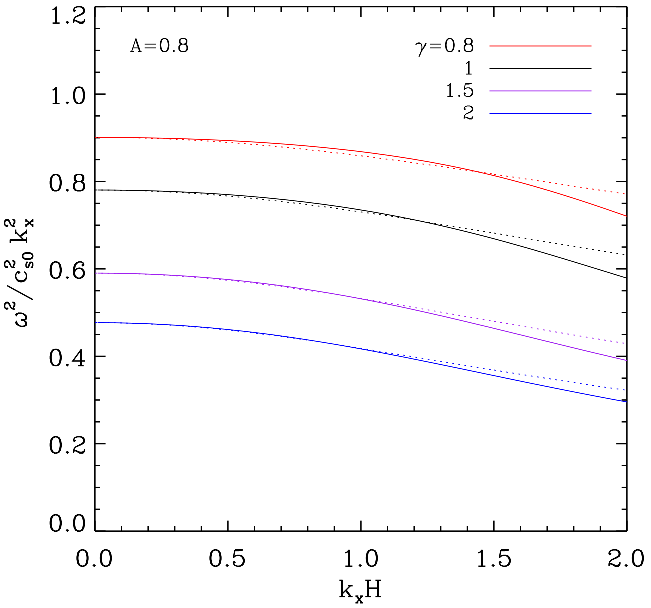

Figure 3. Dispersion relations of the fundamental acoustic-surface-gravity modes in non-self-gravitating, non-rotating, polytropic disks with $\gamma = 0.8, 1, 1.5, 2$. The case with mild pressure-confinement with $A = 0.8$ ($p_{\rm ext}/\pi G\Sigma_0^2 = 0.28$) is shown. The frequency ω is normalized by $c_{s0}k_x$. Solid lines plot the full numerical results, while dotted lines draw the approximate dispersion relation (33).

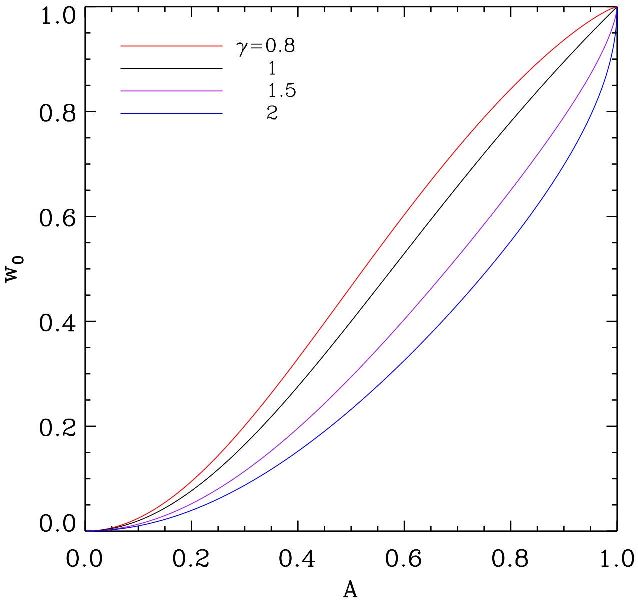

Figure 4. Ratio of the perturbed surface density inside the disk ($\Sigma_{1,i}$) to the total ($\Sigma_{1,i} + \Sigma_{1,s}$) for acoustic-surface-gravity waves in the long wavelength limit as a function of A for differing γ.

ical dispersion relations progressively deviates from the analytic results with increasing k_xH. When $k_xH \lesssim 1$, however, the two agree within $\sim 4\%$ for $0.8 < \gamma < 2$. The agreement becomes better for disks with smaller A. Since GI occurs for waves with $k_xH \lesssim 1$ when self-gravity is included, this suggests that $c_{\rm eff}$ given in equation (30) is a good representative of the averaged sound speed.

3.2. *Free Boundary*

In the case of the free BCs, $\Sigma_{1,s}/\Sigma_{1,i} = \rho_{0a}\xi_{1z}|_{z=a}/\int_0^a \rho_{1,i}\,dz$. Then, the effective sound speed in equation (28) becomes

$$c_{\rm eff}^2 = \left(\frac{\int_{-a}^a \rho_0 h_1/c_s^2\,dz}{\int_{-a}^a \rho_0 h_1\,dz} + \frac{\rho_{0a}h_{1a}}{g_{0a}\int_0^a \rho_0 h_1\,dz} \right)^{-1}, \quad (32)$$

where equation (B3) is used. Equation (32) indicates that waves in a pressure-confined disk with free boundaries make use of two restoring forces: thermal pressure and vertical gravity. The former drives acoustic waves, while the latter is responsible for surface-gravity waves. We term these mixed waves acoustic-surface-gravity waves. The fact that the effective sound speed has two terms, each arising from sound waves and surface-gravity waves, is completely analogous to longitudinal waves propagating in a distensible tube where the effective compressibility of a gas is the sum of the true gas compressibility and the distensibility of the tube (e.g., Lighthill 1978).

Since $\rho_{0a} = \rho_{00}(1 - A^2)^{1/\gamma}$ and $g_{0a} = 4\pi G\rho_{00}AH_0$, it is apparent that the acoustic term in equation (32) dominates for A close to unity. On the other hand, the surface-gravity term becomes important in disks with $A \ll 1$. Appendix E shows that in highly confined disks, even fundamental modes have a particular solution $h_1 \propto \cosh(k_xz)$. Equation (32) is then reduced to

$$c_{\rm eff}^2 = \left(\frac{1}{\tilde{c_s}^2} + \frac{\rho_{0a}/\rho_{00}}{g_{0a}H}\frac{k_xH}{\tanh(k_xH)} \right)^{-1} = w\tilde{c_s}^2, \text{ for free BC}, \quad (33)$$

with w given by equation (26). The sonic contribution $\tilde{c_s}$ is valid for $k_xH \lesssim 1$, as in the rigid BC case. The contribution from surface-gravity waves accounts for the reduced density at the surfaces. In the limit of $A \ll 1$, equations (28) and (33) recover the usual dispersion relation of surface-gravity waves

$$\omega^2 = g_{0a}k_x \tanh(k_xH), \quad (34)$$

in an incompressible medium (e.g., Goldreich & Lynden-Bell 1965a).

Although equation (33) is derived for a disk with either $A \ll 1$ or $A \sim 1$, we find that it is applicable for arbitrary A as long as $k_xH \lesssim 1$. Figure 3 compares equation (33) (dotted lines) with the direct numerical solutions (solid lines) found by solving the full perturbation equations (with self-gravity and rotation neglected) for moderately confined disks with $A = 0.8$ and $\gamma = 0.8$, 1, 1.5, 2. The discrepancies between the two are less than 0.5% for $k_xH \lesssim 1$. This proves that $c_{\rm eff}$ given in equation (33) is excellent in describing the phase velocity of the acoustic-surface-gravity waves in the long-wavelength regime.

From equation (33), it is now clear that the variable w defined by equation (26) is a weight factor representing the relative importance of acoustic to surface-gravity terms in the dispersion relation of acoustic-surface-gravity waves. In the long-wavelength limit, equation (32) leads to

$$w_0 \equiv w|_{k_x\to 0} = \left[1 + \gamma\alpha\frac{(1-A^2)^{1/\gamma}}{2A^2} \right]^{-1}. \quad (35)$$

When $\gamma = 1$, $w_0 = 2A^2/(1+A^2) = (1 + p_{\rm ext}/\pi G\Sigma_0^2)^{-1}$. Figure 4 plots w_0 as functions of A for disks with $\gamma = 0.8$, 1, 1.5, 2. As expected, surface-gravity modes dominate for smaller A and larger γ. From equations (26) and (35), one finds that the mean amplitude of density perturbation inside the disk is given by

$$\frac{\Sigma_{1,i}}{\Sigma_0} = \frac{2A^2}{\gamma\alpha}\frac{\xi_{1z}\big|_{z=a}}{H}, \tag{36}$$

while $\Sigma_{1,s}/\Sigma_0 = (1-A^2)^{1/\gamma}\xi_{1z}\big|_{z=a}/H$ at the disk surfaces. Therefore, $|\Sigma_{1,i}/\Sigma_{1,s}| \ll 1$ for small A. This clearly demonstrates that the fundamental mode and its unstable version (upon inclusion of self-gravity) are incompressible in highly pressure-confined disks (e.g., Elmegreen & Elmegreen 1978; Lubow & Pringle 1993; Nagai et al. 1998; Umekawa et al. 1999).

4. GRAVITATIONAL INSTABILITY

In the preceding section, we derive expressions for the effective sound speed for fundamental acoustic or acoustic-surface-gravity waves in non-self-gravitating and non-rotating disks. In this section, we derive the gravity reduction factors caused by finite disk thickness that explain the numerical dispersion relations of GI fairly well. We begin by considering non-rotating, zero-temperature disks, and then include the effects of thermal pressure and rotation.

4.1. *Pressureless Disks*

Finite disk thickness is known to stabilize the conventional Jeans instability by diluting self-gravity at the disk midplane. As mentioned in Introduction, $\mathcal{F} = (1+k_xH_0)^{-1}$ is often used as the gravity reduction factor for an unbounded, exponential disk with scale height H_0 (e.g., Elmegreen 1982, 1987; Kim et al. 2002). In this subsection, we derive reduction factors for the conventional Jeans modes and the distortional modes in truncated polytropic disks.

We first consider a pressureless, non-rotating disk (i.e., $\widehat{h}_1 = \kappa_0^2 = 0$) for simplicity. For given ρ_1, equation (18) has a formal solution

$$\psi_1(z) = -\frac{2\pi G}{k_x}\int \rho_1(z')e^{-k_x|z-z'|}\,dz', \tag{37}$$

(e.g., Kim & Ostriker 2007). Substituting equation (37) into equation (27), one obtains

$$\omega^2 = -2\pi G\Sigma_0 k_x \mathcal{F}(k_x), \tag{38}$$

where

$$\mathcal{F}(k_x) = \frac{1}{\Sigma_0\Sigma_1}\iint \rho_0(z)\rho_1(z')e^{-k_x|z-z'|}\,dzdz', \tag{39}$$

is the generalized reduction factor of self-gravity at wavenumber k_x. It is apparent from equation (39) that $\mathcal{F} = 1 + O(k_xH)$ in the long wavelength limit, regardless of density distributions.

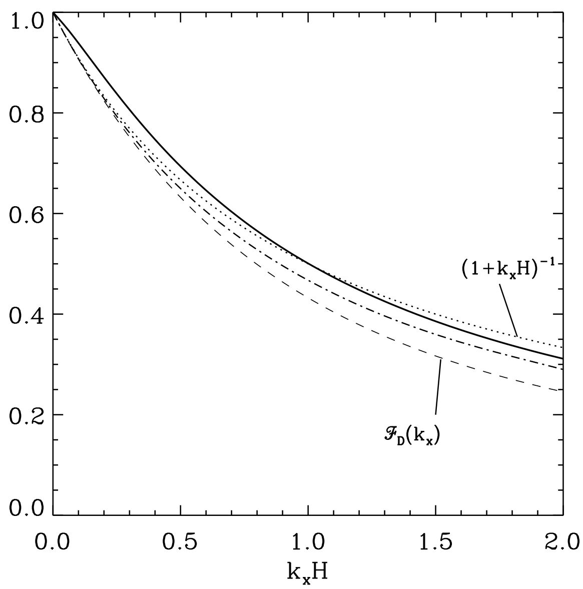

Figure 5. Various gravity reduction factors as functions of k_xH. The solid line plots $\mathcal{F}_{\rm J}$ by taking $\rho_0 \propto {\rm sech}^2(z/H)$ and ρ_1 from the eigensolutions of equations (20)–(23), while the dot-dashed line gives $\mathcal{F}_{\rm J}$ by assuming $\rho_1 \propto \rho_0 \propto {\rm sech}^2(z/H)$. The reduction factor $\mathcal{F}_{\rm D}$ (eq. [45]) of the distortional modes is plotted as a dashed line. For comparison, the commonly used $\mathcal{F} = (1+k_xH)^{-1}$ is plotted as a dotted line.

Using equations (25) and (26), we decompose equation (39) into two parts as

$$\mathcal{F}(k_x) = w\mathcal{F}_{\rm J}(k_x) + (1-w)\mathcal{F}_{\rm D}(k_x), \tag{40}$$

where

$$\mathcal{F}_{\rm J}(k_x) = \frac{1}{\Sigma_0\Sigma_{1,i}}\iint \rho_0(z)\rho_{1,i}(z')e^{-k_x|z-z'|}\,dzdz', \tag{41}$$

and

$$\mathcal{F}_{\rm D}(k_x) = \frac{e^{-k_xa}}{\Sigma_0}\int \rho_0(z)\cosh(k_xz)\,dz, \tag{42}$$

represent the reduction factors of self-gravity for the conventional Jeans modes and distortional modes, respectively.

We integrate equation (41) for an unbounded ($A=1$), isothermal disk with $\rho_0 \propto {\rm sech}^2(z/H_0)$. The resulting $\mathcal{F}_{\rm J}$ with $\rho_{1,i} \propto \rho_0$ is plotted in Figure 5 as a dot-dashed line, while the case with $\rho_{1,i}$ numerically obtained from the full solution of equations (20)–(23) is shown as a solid line. Note that both are closely approximated by $(1 + k_xH)^{-1}$ shown as a dotted line. For pressure-confined disks, we empirically found by varying A as well as the BCs that

$$\mathcal{F}_{\rm J} = \frac{1}{1+k_xHA^{1/2}}, \quad \text{for rigid BC}, \tag{43}$$

and

$$\mathcal{F}_{\rm J} = \frac{1}{1+k_xH}, \quad \text{for free BC}, \tag{44}$$

match the numerical dispersion relations of GI quite well (see below).[1] The difference between equations (43) and

---

[1] For an unbounded, exponential disk with $\rho_0 \propto \rho_{1,i} \propto \exp(-|z|/H)$, equation (41) yields

$$\mathcal{F}_{\rm J}^{\rm exp} = \frac{1}{1+k_xH} - \frac{k_xH}{2(1+k_xH)^2},$$

which is different from the often-used expression (eq. [44]). The latter is in fact the exact force correction term *at* the $z=0$ plane (e.g., Kim & Ostriker 2007), while the former is the correction factor *averaged* along the z-direction. Nevertheless, equation (44) matches the reduction factor for ${\rm sech}^2(z/H)$ disks better than $\mathcal{F}_{\rm J}^{\rm exp}$.

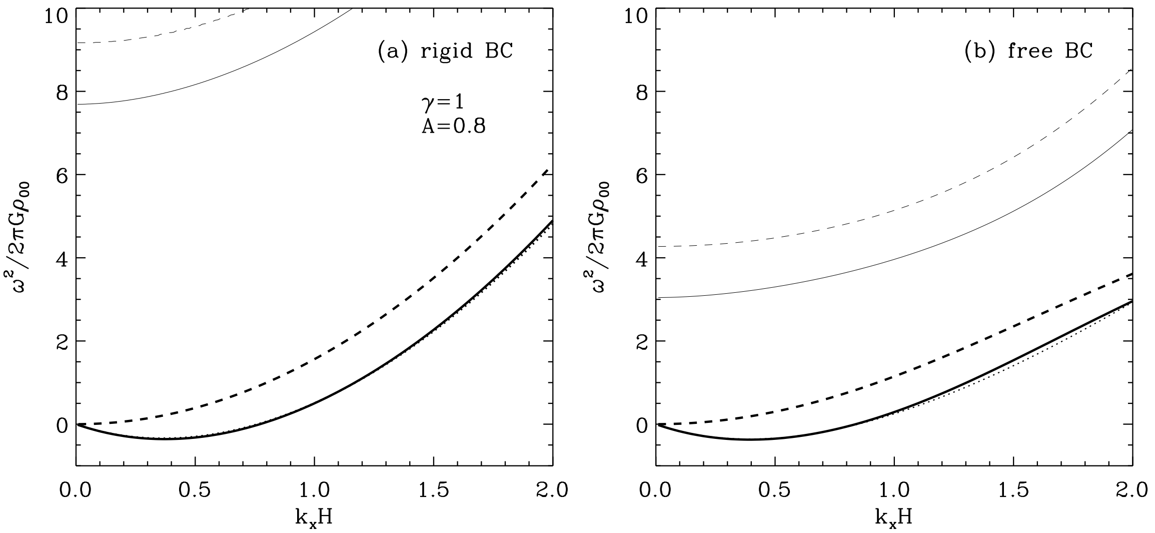

Figure 6. Dispersion relations of the fundamental modes (thick lines) and the first harmonics (thin lines) of the (a) acoustic and (b) acoustic-surface-gravity waves in disks with $A = 0.8$ and $\gamma = 1$. Solid and dashed lines plot the numerical results with and without self-gravity, respectively, while dotted lines draw the approximate dispersion relation (eq. [46]) for the fundamental modes.

(44) is due to the fact that $\rho_{1,i}$ in equation (41) is affected by the BCs.

For small A, $\mathcal{F}$ is mostly from $\mathcal{F}_{\rm D}$ (see eq. [40]). In this case, the distortional modes resulting from $\rho_{1,s}$ dominate, and it is reasonable to take $\rho_0 \approx$ constant and $a \approx H$ in the evaluation of $\mathcal{F}_{\rm D}$. Equation (42) then becomes

$$\mathcal{F}_{\rm D} = e^{-k_x a}\frac{\sinh k_x H}{k_x H}, \tag{45}$$

which is plotted as a dashed line in Figure 5. Incidentally, $\mathcal{F}_{\rm D}$ is not much different from $(1 + k_x H)^{-1}$, either.

4.2. *Non-rotating Disks*

We now explore GI of non-rotating, pressure-confined disks with the effect of thermal pressure included. Combining the results of Sections 3 and 4.1, we write an approximate dispersion relation

$$\omega^2 = c_{\rm eff}^2 k_x^2 - 2\pi G\Sigma_0 k_x (w\mathcal{F}_{\rm J} + (1-w)\mathcal{F}_{\rm D}), \tag{46}$$

where $c_{\rm eff}$ is given by either equation (30) or equation (33) depending on the BCs.

4.2.1. *Rigid Boundary*

First, we impose the rigid BCs with $w = 1$. Figure 6a plots the dispersion relations of waves with (solid lines) and without (dashed lines) self-gravity in disks with $\gamma = 1$ and $A = 0.8$ for the fundamental acoustic modes (thick) as well as the first harmonics (thin) obtained numerically by solving the perturbation equations (20)–(23). The approximate dispersion relation (46) for the fundamental mode is plotted as dotted lines, which are in good agreement with the numerical results for $k_x H \lesssim 2$. Clearly, self-gravity lowers the frequency and it is the fundamental mode that becomes unstable upon inclusion of self-gravity. GI under the rigid BCs is the conventional Jeans instability since surface distortion is absent.

Figure 7 plots as solid lines the numerical dispersion relations of pure Jeans modes for some selected values of A and γ, which agree quite well with equation (46) drawn as dotted lines: the relative differences between the true and approximate values of the maximum growth rates and critical wavenumbers are less than 5% for $0.8 \le \gamma \le 2$ and $0 \le A \le 1$. For fixed Σ_0 and c_{s0}, the Jeans modes are more unstable for smaller A because the disk becomes geometrically thinner. In the limit of $A \to 0$, the dispersion relations of GI in pressure-confined disks become identical to those of an infinitesimally-thin disk with the same Σ_0 and c_{s0}, shown as dashed lines in Figure 7a-c. For fixed A, disks with larger γ are more unstable owing to a steeper temperature gradient as well as a smaller vertical scale height ($H_0 = Ac_{s0}^2/(\pi G\Sigma_0\gamma) \propto \gamma^{-1}$). Figure 7d replots Figure 7a by scaling ω and k_x in terms of $c_{\rm eff}$ rather than the midplane sound speed c_{s0}. Close agreement among the curves with different γ evidences that the effective sound speed defined in equation (30) is really a good representative of the mean averaged sound speed of polytropic disks.

4.2.2. *Free Boundary*

Under the free BCs, perturbations experience two types of restoring forces: compressibility and surface gravity. The former and latter dominate when $A \sim 1$ and $A \ll 1$, respectively. For general A, these are mixed together to become acoustic-surface-gravity waves. Figure 6b plots the numerical (solid lines) and approximate (dotted lines; eq. [46]) dispersion relations for the fundamental modes (thick) and the first harmonics (thin) in disks with $A = 0.8$ and $\gamma = 1$. Non-self-gravitating waves are plotted as dashed lines, while solid lines draw the self-gravitating waves. The close agreement between the numerical and analytic results shows that the fundamental modes under the free BCs are really acoustic-surface-gravity waves that become unstable when self-gravity is included. In what follow, we call the unstable acoustic-surface-gravity modes the mixed GI. Figure 8 plots as solid lines the numerical dispersion relations of the acoustic-surface-gravity modes in non-rotating, pressure-confined disks with various values of A and

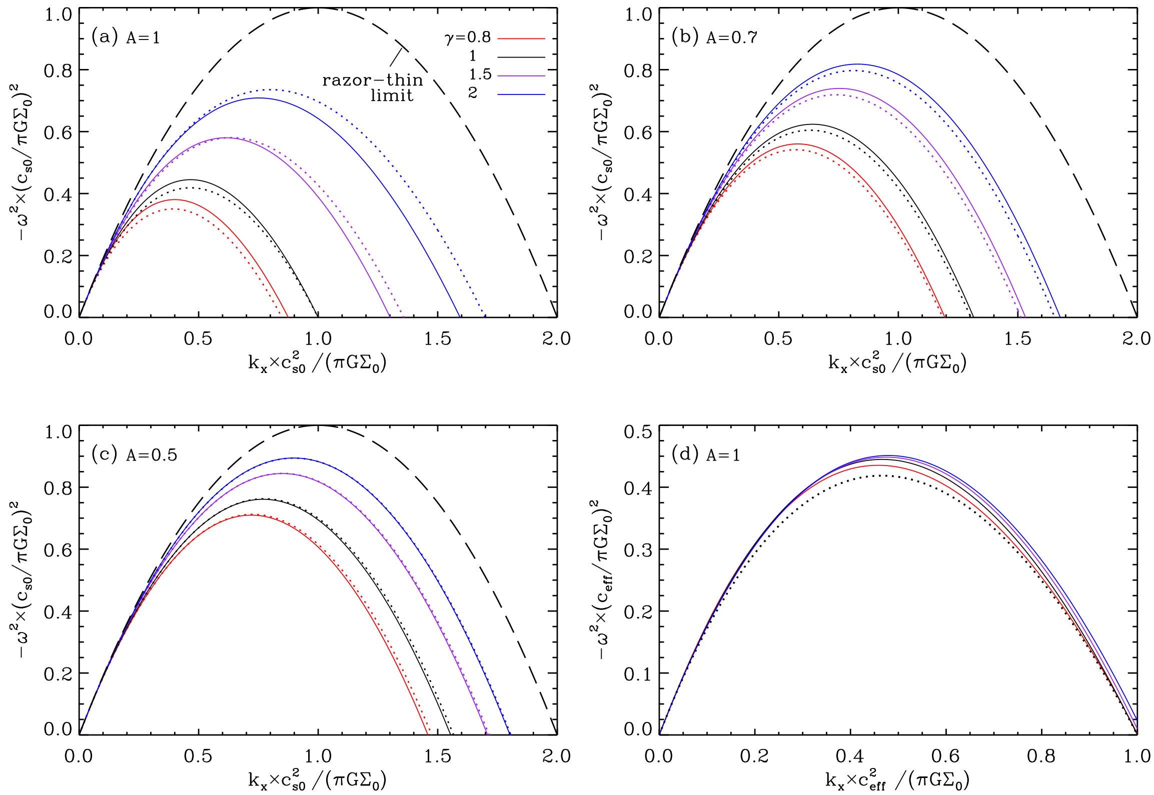

Figure 7. (a)–(c): Dispersion relations of the pure Jeans modes in non-rotating, pressure-confined, polytropic disks under the rigid BCs. The wavenumber and growth rate are normalized by using the midplane sound speed. The solid lines are the numerical results, while the approximate dispersion relations (eq. [46]) are plotted as dotted lines. The razor-thin dispersion relation ($A \to 0$) is shown as a long dashed line in each panel. (d): The $A = 1$ case plotted in (a) is redrawn using $c_{\rm eff}$ in the normalization of ω and k_x.

γ. The wavenumber and growth rate are normalized by the effective half-thickness H and the free-fall time at the midplane, $(2\pi G\rho_{00})^{-1/2}$, respectively. The cases with $\gamma = 1$ recover the results of earlier studies (e.g., Simon 1965; Elmegreen & Elmegreen 1978; Usami et al. 1995; Iwasaki et al. 2011). Shown also as dotted lines are the approximate dispersion relation in good agreement with the numerical results. Regardless of A, the maximum growth rate, $|\omega_{\rm max}|$, of unstable modes occurs at $kH \sim 0.3$–0.4. However, the physical nature of GI is markedly different depending on the degree of pressure confinement. When the external pressure is weak ($A \approx 1$), unstable modes are dominated by acoustic-type perturbations ($w \sim 1$), making the mixed GI under the free BCs similar to the pure Jeans mode occurring under the rigid BCs. When perturbations from surface distortion dominate ($A \ll 1$), on the other hand, equation (46) is reduced to

$$\omega^2 = g_{0a}k_x \tanh(k_xH) - 2\pi G\Sigma_0 k_x \times \frac{1-e^{-2k_xH}}{2k_xH}, \quad (47)$$

for the pure distortional instability (e.g., Goldreich & Lynden-Bell 1965a).

Figure 9 compares the marginal wavenumber $k_{x,c}$, the most unstable wavenumber $k_{x,\rm max}$, and the maximum growth rate $\omega_{\rm max}$ of the pure Jeans instability with those of the mixed GI of isothermal disks as functions of A. The mixed GI is identical to the pure Jeans mode when $A = 1$, but the former in general has a higher growth rate and occurs at a shorter wavelength than the latter for arbitrary A. This is because the effective sound speed varies with A differently depending on the BCs. For $A \ll 1$, $c_{\rm eff} \sim c_{s0}$ for the pure Jeans modes (eq. [31]), while $c_{\rm eff} \sim \sqrt{g_{0a}a} \propto A$ for the mixed GI (eq. [33]). Since both types of GI have the characteristic wavenumber $k_{x,c} \sim \pi G\Sigma_0/c_{\rm eff}^2$ and growth rate $|\omega| \sim k_{x,c}/c_{\rm eff}$, the critical wavenumber and maximum growth rate of the Jeans modes are smaller by a factor of A^2 and A, respectively, compared to those of the mixed GI.

4.3. *Rotating Disks and Stability Criteria*

Finally, we include the effect of disk rotation and study the stability condition to axisymmetric GI. In view of equation (27), one may assume that the gas motions arising from thermal pressure and self-gravity are separable from the epicycle motions, which is shown valid for $k_xH \lesssim 1$ in the preceding sections. The approximate dispersion relation of GI then becomes

$$\omega^2 = c_{\rm eff}^2 k_x^2 - 2\pi G\Sigma_0 k_x \mathcal{F}(k_x) + \kappa_0^2, \quad (48)$$

which is a generalization of equation (1) to pressure-confined, polytropic disks with vertical stratification. Figure 10 compares equation (48) shown as dotted lines with the full numerical results plotted as solid lines for disks with $A = 0.7$, $\gamma = 0.8$, 1, 1.5, 2, and $\kappa_0^2 = 0.2(\pi G\Sigma_0/c_{s0})^2$, which are in good agreement with each other, demonstrating again that equation (48) is accurate in describing GI of pressure-confined polytropic disks

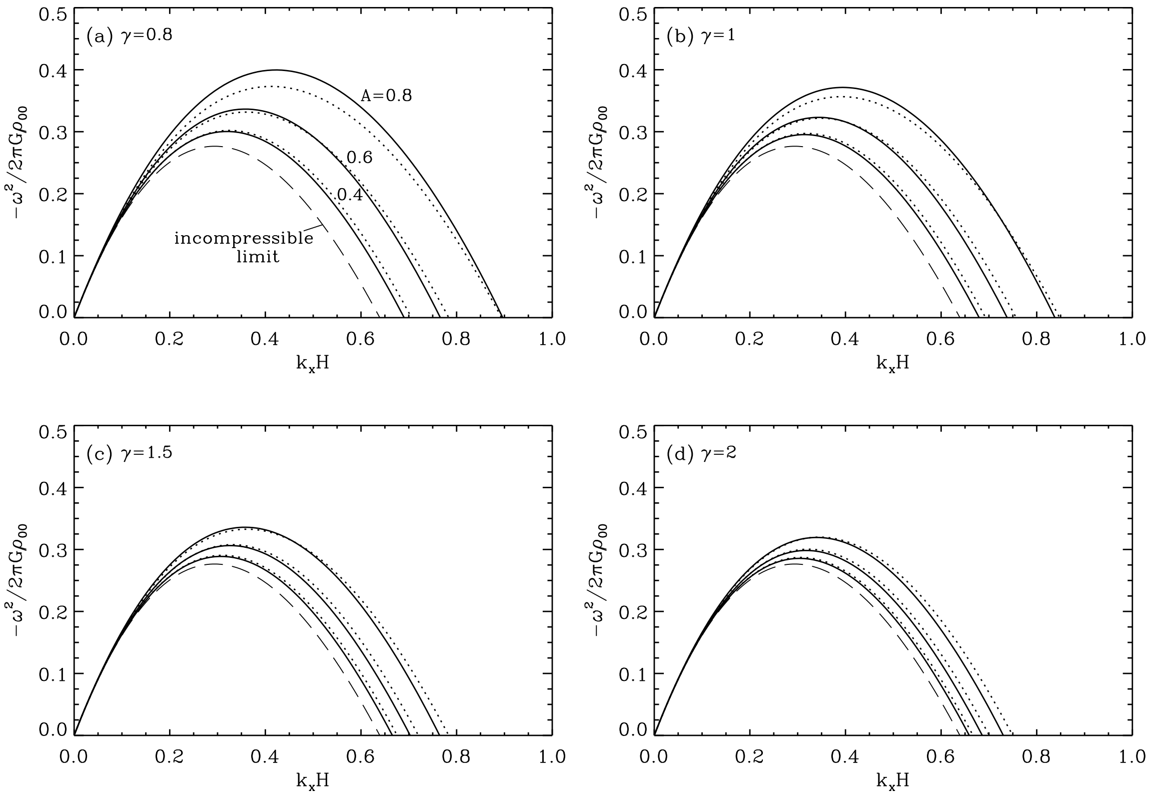

Figure 8. Dispersion relations of the mixed GI in non-rotating, pressure-confined polytropic disks with $\gamma = 0.8, 1, 1.5, 2$ and $A = 0.4, 0.6, 0.8$ under the free BCs. Solid lines draw the numerical results, while dotted lines plot the approximate dispersion relation (eq. [46]). In each panel, the pure distortional modes in the limit of $A \to 0$ are shown as a long dashed line.

provided $c_{\rm eff}$ and $\mathcal{F}$ are chosen appropriately.

We generalize Toomre's stability parameter originally defined for a razor-thin disk to vertically-stratified, pressure-confined disks as

$$Q_{\rm eff} \equiv \frac{c_{\rm eff}\kappa_0}{\pi G \Sigma_0}. \tag{49}$$

Using $c_{\rm eff}/H_0 = (2\alpha\gamma\pi G\rho_{00})^{1/2}$ for $A = 1$, one can show that the stability parameter $Q_M = \Omega^2/(4\pi G\rho_{00})$ used by Mamatsashvili & Rice (2010) is equal to $\sqrt{Q_{\rm eff}/(8\alpha\gamma)}$. Since $\mathcal{F} \lesssim 1$, the critical value of $Q_{\rm eff}$ is less than unity. Note that in the limit of strong pressure confinement, $Q_{\rm eff}$ is reduced to

$$Q_{\rm eff} \to \frac{\sqrt{g_{0a}a}\,\kappa_0}{\pi G\Sigma_0} = \frac{\kappa_0}{\sqrt{\pi G\rho_{00}}}, \quad \text{for } A \to 0, \tag{50}$$

applicable to the pure distortional modes.

Figure 11 plots the critical values $Q_{{\rm eff},c}$ for axisymmetric GI in the (γ, A) plane. Figure 11a is for pure Jeans instability under the rigid BCs, while the case of mixed GI with the free BCs is shown in Figure 11b. As $A \to 0$, $Q_{{\rm eff},c}$ always converges to 1, for pure Jeans modes, corresponding to a razor-thin disk, and to 0.756 for the mixed GI, corresponding to an incompressible disk (Goldreich & Lynden-Bell 1965a). In the pure Jeans instability, finite disk thickness weakens self-gravity, decreasing $Q_{{\rm eff},c}$ with increasing A. For example, an unbounded isothermal disk has $Q_{{\rm eff},c} = 0.676$ (Goldreich & Lynden-Bell 1965a). For the mixed GI, $Q_{{\rm eff},c} \sim 0.68$–$0.75$ largely insensitive to γ.

5. SUMMARY AND DISCUSSION

We investigate GI of rotating, pressure-confined, vertically-stratified gas disks to axisymmetric perturbations. As an initial equilibrium, we consider a self-gravitating, polytropic disk in hydrostatic equilibrium. The disk is truncated by a constant external pressure characterized by a dimensionless parameter A (eq. [14]). To distinguish distortional modes of GI occurring in highly confined disks from the conventional Jeans modes, we adopt the rigid-surface BCs that allow only Jeans modes as well as the free-surface BCs under which two modes coexist. Our model disks do not include convective motions.

By deriving approximate dispersion relations and comparing them with the numerical results from a set of the perturbation equations (20)–(23), we find that GI-unstable modes are in general even-symmetry fundamental modes that have no vertical node. Under the rigid BCs, the fundamental modes are simply acoustic waves that propagate via thermal pressure only. Under the free BCs, on the other hand, surface-gravity waves arising from surface distortion provide an additional restoring force, forming acoustic-surface-gravity waves. In the presence of self-gravity, the acoustic waves become unstable to pure Jeans modes, while the surface-gravity waves become unstable to incompressible, distortional modes. Therefore, disks under the free BCs are unstable to the mixed GI in which the Jeans and distortional modes coexist. When pressure confinement is weak ($A \sim 1$), the Jeans modes dominate, while the distortional modes be-

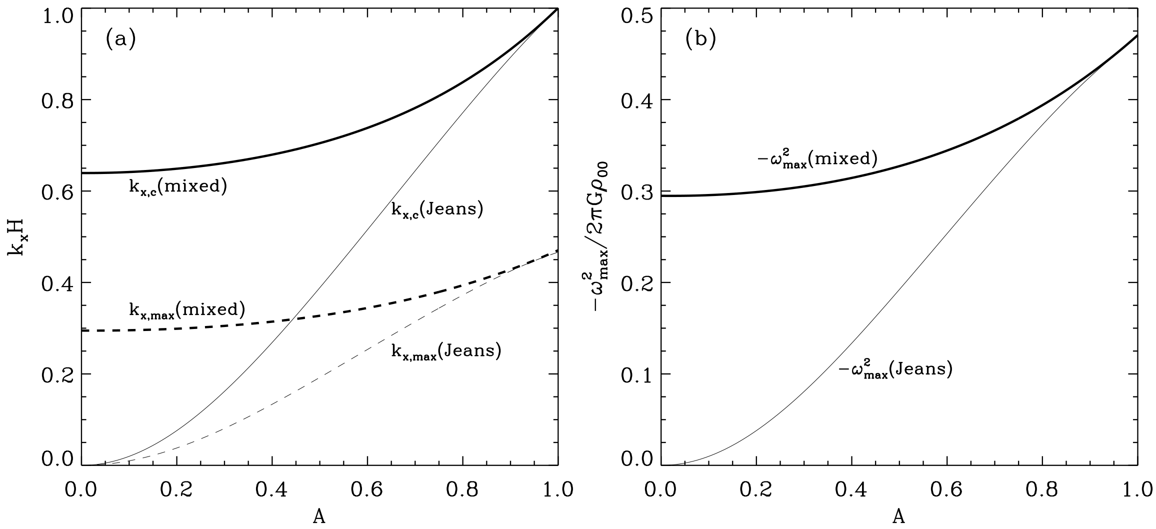

Figure 9. (a) Maximum ($k_{x,\rm max}$; dashed lines) and critical ($k_{x,c}$; solid lines) wavenumbers, and (b) squared maximum growth rate as functions of A for $\gamma = 1$. The thick lines correspond to the mixed GI under the free BCs, while the thin lines are for the pure Jeans modes under the rigid BCs.

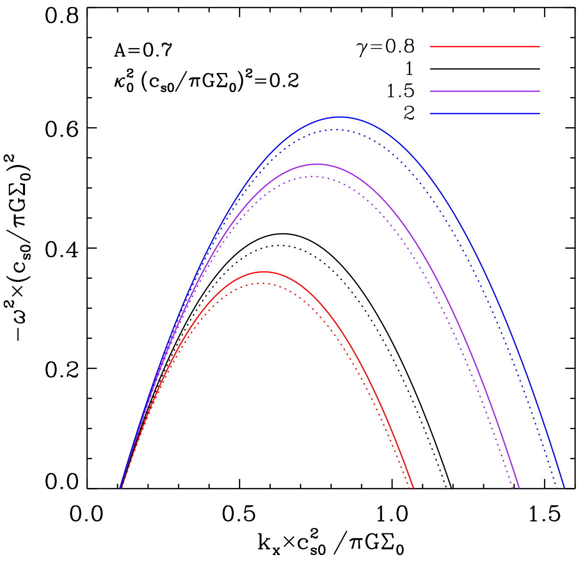

Figure 10. Dispersion relations of rotating, polytropic disks with $A = 0.7$ and $\gamma = 0.8$, 1, 1.5, 2 when $\kappa_0^2 = 0.2\,(\pi G\Sigma_0/c_{s0})^2$. Solid lines plot the numerical results, while dotted lines draw the approximate dispersion relation (eq. [48]).

come prevalent in strongly confined disks. The relative importance of the Jeans modes can be measured by the dimensionless parameter w_0 defined by equation (35).

While polytropic disks are vertically stratified both in density and temperature, we find that the effective sound speed $c_{\rm eff}$ defined either by equation (30) for the rigid BCs or equation (32) for the free BCs represents the mean propagation speed of acoustic-surface-gravity waves quite well. Under the rigid BCs, $c_{\rm eff}$ is given by the density-weighted, harmonic mean of the local sound speeds, while it has a contribution from the surface-gravity waves under the free BCs.

We derive the reduction factors $\mathcal{F}(k_x)$ responsible for the reduced gravity due to finite disk thickness for the pure Jeans modes (eqs. [43] and [44]) and for the distortional modes (eq. [45]). The approximate dispersion relation (48) matches the numerical results very closely as long as the effective sound speed and the gravity reduction factors are properly chosen. Disk rotation introduces inertial waves associated with epicyclic motion, but it is again the fundamental mode of acoustic-surface-gravity waves that are subject to GI. Using the effective sound speed, we define the stability parameter $Q_{\rm eff}$ as in equation (49) that generalizes the Toomre's parameter into pressure-confined, polytropic disks. The pure Jeans modes have the critical values $Q_{{\rm eff},c} = 0.67 - 1$ with the larger value corresponding to a razor-thin disk, while the mixed GI has $Q_{{\rm eff},c} = 0.67 - 0.76$ insensitive to γ.

As mentioned in Introduction, the origin of the mixed GI of pressure-confined disks has been uncertain. Various mechanisms such as neutral modes (Lubow & Pringle 1993), pinching force (Elmegreen 1989; Umekawa et al. 1999; Wünsch et al. 2010), and surface-gravity waves (Iwasaki et al. 2011) have been proposed as the cause of GI. In this paper, we clearly show that the mixed GI occurring under the free BCs is a combination of pure Jeans and distortional modes, the latter of which is generated by deformation of free surfaces. The existence of an additional restoring force due to the vertical gravity excites low-frequency fundamental modes, as opposed to high-frequency acoustic modes. With a reduced effective sound speed, the mixed GI has a larger growth rate and a smaller length scale than the pure Jeans modes.

Recently, Iwasaki et al. (2011) performed a linear stability analysis of expanding isothermal shells around H II regions. They considered combinations of the rigid and free BCs as well as an asymmetric density profile caused by the bulk deceleration of a shell. They found that the numerically calculated dispersion relations are well described by an approximate relation $\omega^2 = c_{{\rm eff},I}^2 k_x^2 - 2\pi G\Sigma_0 k_x$, where $c_{{\rm eff},I}^2 = [B \times 4\pi G\Sigma_0 H + (c_s/2)^2]$. Although the dimensionless parameter $B = 0.39$ in their effective sound speed $c_{{\rm eff},I}$ gives the best fit to their

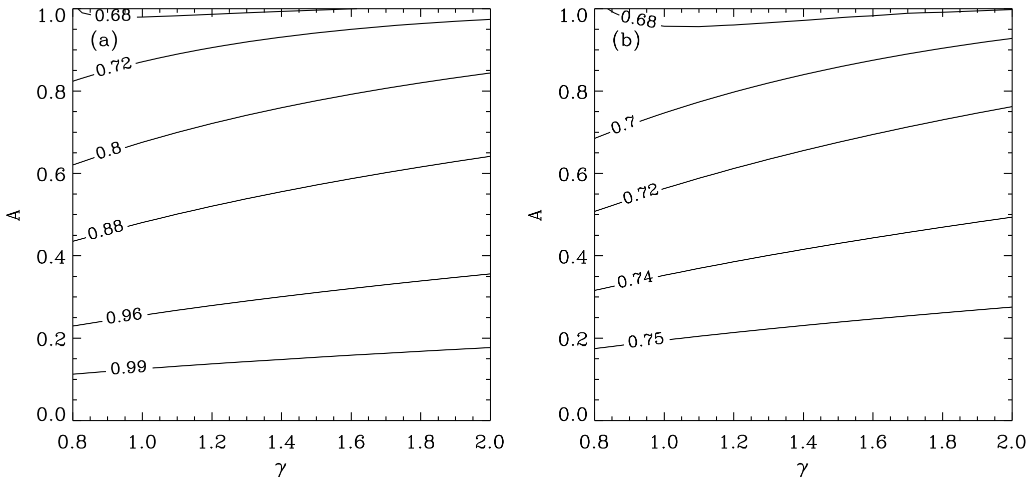

Figure 11. Contours of the critical $Q_{\rm eff}$ values of (a) the pure Jeans modes under the rigid BCs and (b) the mixed GI under the free BCs for pressure-confined, polytropic disks. As $A \to 0$, $Q_{\rm eff,c}$ approaches unity for the pure Jeans modes and 0.756 for the mixed GI, independent of γ.

numerical growth rates, its physical nature is somewhat ambiguous. Noting that $H = A^2c_s^2/(\pi G\Sigma_0)$, the above relation can be arranged as $\omega^2 = c_{\rm eff}^2 k_x^2 - 2\pi G\Sigma_0 k_x \mathcal{F}_{\rm I}(k_x)$, similarly to equation (46), with the effective sound speed of acoustic-surface-gravity waves $c_{\rm eff} = 2A^2/(1+A^2)c_s^2$ in the long-wavelength limit (eq. [33]) and the gravity reduction factor modified to $\mathcal{F}_{\rm I}(k_x) = 1 - k_xH \times [2B + (1-7A^2)/(8A^2(1+A^2))]$. For $A \gtrsim 0.4$ (or, $p_{\rm ext}/(\pi G\Sigma_0) \lesssim 21/8$) considered by Iwasaki et al. (2011), $\mathcal{F}_{\rm I} = 1 - (0.4$–$0.6)k_xH$ in reasonable agreement with the reduction factors that we found (see Figure 5). This suggests that $c_{{\rm eff},I}$ in the approximate dispersion relation of Iwasaki et al. (2011) contains a contribution from the reduced gravity due to finite shell thickness.

While the mixed GI of pressure-confined disks has received a little attention compared to pure Jeans modes, it may be responsible for structure formation via fragmentation of thin shells in the ISM. For example, Boyd & Whitworth (2005) claimed that GI of shock-compressed layers can explain the formation of Jupiter-mass (significantly smaller than the Jeans mass) objects detected in young star clusters (Zapatero Osorio et al. 2002). Recently, Wünsch et al. (2012) reported that the observed slopes of the mass spectrum of molecular clouds in the Carina Flare are indeed consistent with those expected from GI of pressure-confined shells. Distortional modes in flattened systems can be thought of as arising from the tendency to lower the gravitational potential energy by transforming into a spherical configuration (Usami et al. 1995). Thus, the mixed GI would occur not only in a planar geometry but also in a cylindrical gaseous column. In the presence of magnetic fields, distortional instability is suppressed in the direction parallel to the magnetic fields (Nagai et al. 1998), naturally leading to cloud formation in filamentary shapes.

We are grateful to the referee for a helpful report. This work was supported by the National Research Foundation of Korea (NRF) grant funded by the Korean government (MEST), No. 2010-0000712.

APPENDIX

A. HYDROSTATIC EQUILIBRIUM

In this appendix, we derive an analytic solution of equations (7) and (8) for the density distributions of self-gravitating polytropic disks. We begin by defining the dimensionless variables

$$\xi = z/H_0, \tag{A1}$$

$$\Theta(\xi) = (\rho_0/\rho_{00})^{1/n}, \tag{A2}$$

where $n \equiv 1/(\gamma - 1)$ is the polytropic index. Then, equations (7) and (8) result in

$$\frac{d^2\Theta}{d\xi^2} = -\left(\frac{2}{1+n}\right)\Theta^n. \tag{A3}$$

Equation (A3) is the usual Lane-Emden equation in the planar geometry (e.g., Viala & Horedt 1974), which can be solved with the proper boundary conditions $\Theta(0) = 1$ and $d\Theta(0)/d\xi = 0$.

Now, we combine equations (8) and (9) together with equations (A1) and (A2) to obtain

$$\frac{d}{d\xi} = \Theta^n \frac{d}{d\mu}. \tag{A4}$$

On the other hand, by integrating equation (8) over z and using equation (A3), we express μ in equation (9) as

$$\mu = -\left(\frac{1+n}{2}\right)\frac{d\Theta}{d\xi} = -\left(\frac{n+1}{2}\right)\Theta^n\frac{d\Theta}{d\mu}, \tag{A5}$$

where the second equality utilizes equation (A4). The solution of equation (A5) that satisfies the boundary conditions is simply

$$\Theta = (1-\mu^2)^{1/(n+1)}, \tag{A6}$$

or

$$\rho_0(\mu) = \rho_{00}(1-\mu^2)^{1/\gamma}, \tag{A7}$$

(see also, Harrison & Lake 1972).

To find ρ_0 in terms of z, we substitute equations (A1) and (A6) into equation (A4) to obtain

$$\frac{z}{H_0} = \int_0^\mu \frac{d\mu}{(1-\mu^2)^{1/\gamma}}. \tag{A8}$$

A formal solution of equation (A8) is given by

$$\frac{z}{H_0} = {}_2F_1\left(\tfrac{1}{2}, \tfrac{1}{\gamma}; \tfrac{3}{2}; \mu^2\right)\mu, \tag{A9}$$

where ${}_2F_1$ denotes the Gaussian hypergeometric function. Equation (A8) is integrable for a few particular values of γ:

1. When $\gamma = 2/3$,
$$z/H_0 = \mu/\sqrt{1-\mu^2}, \quad \text{and} \quad \rho_0 = \rho_{00}\left(1+(z/H_0)^2\right)^{-3/2}, \tag{A10}$$
where $H_0^2 = K/(2\pi G\rho_{00}^{4/3})$ (e.g., Larson 1985).
2. When $\gamma = 1$,
$$z/H_0 = \tanh^{-1}\mu, \quad \text{and} \quad \rho_0 = \rho_{00}\mathrm{sech}^2(z/H_0), \tag{A11}$$
where $H_0^2 = K/(2\pi G\rho_{00})$ (e.g., Ledoux 1951; Goldreich & Lynden-Bell 1965a).
3. When $\gamma = 2$,
$$z/H_0 = \sin^{-1}\mu, \quad \text{and} \quad \rho_0 = \rho_{00}\cos(z/H_0), \tag{A12}$$
where $H_0^2 = K/(2\pi G)$ (e.g., Goldreich & Lynden-Bell 1965a).
4. When $\gamma = \infty$,
$$z/H_0 = \mu, \quad \text{and} \quad \rho_0 = \rho_{00}, \tag{A13}$$
(e.g., Harrison & Lake 1972).

B. BOUNDARY CONDITIONS

Equations (20)–(23) possess a reflection symmetry with respect to the $z = 0$ plane, that is, invariant under the transformations $z \to -z$, $\xi_{1z} \to -\xi_{1z}$, $\psi_1' \to -\psi_1'$, $h_1 \to h_1$, $\psi_1 \to \psi_1$. Thus, perturbations are in general a superposition of even-symmetry modes and odd-symmetry modes. Of these, odd-symmetric modes satisfying $\xi_{1z}(z) = \xi_{1z}(-z)$, $h_1(z) = -h_1(-z)$, $\psi_1(z) = -\psi_1(-z)$, $\psi_1'(z) = \psi_1'(-z)$ are shown to be stable against GI (e.g. Simon 1965; Elmegreen & Elmegreen 1978; Mamatsashvili & Rice 2010). Therefore, we in this work consider only even-symmetry modes for which it is suffice to write only two conditions

$$\xi_{1z}(0) = \psi_1'(0) = 0. \tag{B1}$$

The other two conditions on $h_1(0)$ and $\psi_1(0)$ are automatically satisfied from equations (20)–(23).

At the boundaries truncated by the external pressure, we consider two different types of BCs: the rigid and free conditions. In the rigid BC, the boundaries are assumed to be fixed with a vanishing Lagrangian displacement

$$\xi_{1z}\big|_{z=a} = 0, \quad \text{for rigid BC}, \tag{B2}$$

(e.g., Voit 1988). This condition may be appropriate to describe boundaries of a thin layer, as produced by colliding clouds, since the shocked interfaces are stable against distortion (Usami et al. 1995; Iwasaki et al. 2011).

The free BC allows for a deformed Lagrangian surface on which the pressure is maintained constant to its initial value $p_{\rm ext}$ (Goldreich & Lynden-Bell 1965a; Elmegreen & Elmegreen 1978; Lubow & Pringle 1993; Iwasaki et al. 2011). Since $p_{\rm ext} = p(a + \xi_{1z}|_{z=a}) = p_0|_{z=a} + p_1|_{z=a} + (\xi_{1z}\, dp_0/dz)_{z=a}$ to first order, one obtains

$$h_1\big|_{z=a} = g_{0a}\xi_{1z}\big|_{z=a}, \quad \text{for free BC}, \tag{B3}$$

where $g_{0a} \equiv d\psi_0/dz\big|_{z=a}$ is the vertical gravity at the disk boundary (e.g., Goldreich & Lynden-Bell 1965a).

In self-gravitating disks, another condition comes from applying the divergence theorem to the perturbed Poisson equation at the interface. Integrating equation (18) over the volume of a thin shell placed at the interface gives

$$- k_x\psi_1|_{z=a} - \frac{d\psi_1}{dz}\bigg|_{z=a} = 4\pi G\rho_0\xi_{1z}\big|_{z=a}, \tag{B4}$$

where the relation $d\psi_1/dz|_{z=a+} = -k_x\psi_1|_{z=a}$ is used since the gravitational potential outside the disk satisfies Laplace's equation.

C. METHOD OF NUMERICAL INTEGRATION

For a given set of disk parameters (γ, A, κ_0^2), we wish to find a dispersion relation $\omega = \omega(k_x)$ that satisfies the perturbations equations (20)–(23) subject to the two BCs and two even-symmetry constraints. Since the perturbation equations are linear in terms of the independent variables $(\xi_{1z}, h_1, \psi_1, \psi_1')$, we are free to choose one of the variables arbitrarily. We thus fix $h_1|_{z=a} = 1$ (or $\xi_{1z}|_{z=a} = 1$) and take trial values for $\psi_1|_{z=a}$ and ω^2, while obtaining $\xi_{1z}|_{z=a}$ (or $h_1|_{z=a}$) and $\psi_1'|_{z=a}$ from equations (B2)–(B4) depending on the adopted BCs. We then integrate equations (20)–(23) from $z = a$ to $z = 0$ using the fourth-order Runge-Kutta-Gill method (Abramowitz & Stegun 1972). At the $z = 0$ plane, we check the even-symmetry conditions (B1): if these are not fulfilled, we go back to the disk boundary, change $\psi_1|_{z=a}$ and ω^2 slightly based on the Newton-Raphson technique, and repeat the integrations. Solutions with accuracy of 10^{-4}, that is, with $|\xi_{1z}(0)/\xi_{1z}(a/2)|, |\psi_1'(0)/\psi_1'(a)| < 10^{-4}$ are obtained typically within less than three iterations.

D. MODE CLASSIFICATION AND EFFECTS OF SELF-GRAVITY

Here, we first derive local dispersion relations of waves in the WKB limit, and compare them with the numerical results. This will help us verify that acoustic modes become unstable in the presence of self-gravity. We then discuss our results in comparison with the results of Mamatsashvili & Rice (2010) who mistakenly claimed that gravity makes inertial modes unstable.

D.1. *Local Analysis*

We seek for the solutions of equations (20)–(23) for local waves with $k_x, k_z \gg H_0^{-1}$. Defining $k_z^2 \equiv -\chi_1^{-1}d^2\chi_1/dz^2$ with $\chi_1 = h_1 + \psi_1$, it is straightforward to derive

$$\omega^4 - \omega^2(\beta c_s^2 k^2 + \kappa_0^2) + \kappa_0^2\,\beta c_s^2 k_z^2 = 0, \tag{D1}$$

where $k^2 = k_x^2 + k_z^2$ and $\beta \equiv 1 + \psi_1/h_1 = 1 - 4\pi G\rho_0/(c_s^2 k^2)$ is the correction factor for self-gravity (e.g., Chandrasekhar 1961). The corresponding eigenfunctions are

$$\begin{pmatrix} \rho_1/\rho_0 \\ u_{1x}/c_s \\ u_{1z}/c_s \end{pmatrix} = \mathcal{A} \begin{pmatrix} 1 \\ -\beta\omega c_s k_x/(\omega^2 - \kappa_0^2) \\ -\beta c_s k_z/\omega \end{pmatrix} e^{i(\omega t + k_x x + k_z z)}, \tag{D2}$$

where $\mathcal{A}$ is an arbitrary constant.

For waves with $|\beta| c_s^2 k^2 \gg \kappa_0^2$ or $k \gg k_z$, equation (D1) yields two approximate solutions

$$\omega_p^2 = \beta c_s^2 k^2 + \kappa_0^2, \tag{D3}$$

$$\omega_r^2 = \kappa_0^2 \frac{\beta c_s^2 k_z^2}{\beta c_s^2 k^2 + \kappa_0^2}. \tag{D4}$$

It can be shown that the group and phase velocities of the waves associated with ω_p^2 are parallel to each other, while those with ω_r^2 are perpendicular. This demonstrates that the former is acoustic waves (p modes) boosted by epicycle motions, while the latter is inertial waves (r modes). Note that inertial waves require non-vanishing k_z for propagation.

It is apparent from equation (D3) that the local acoustic waves become gravitationally unstable provided self-gravity is sufficiently strong with $\beta < -\kappa_0^2/(c_s^2 k^2)$. On the other hand, the inertial waves usually have $k_z H_0 \gg 1$ so that $\omega_r^2 \approx \kappa_0^2 k_z^2/k^2$ regardless of β, indicating that the character and frequencies of inertial waves are almost unchanged by self-gravity. Figure 12 demonstrates this by directly comparing equations (D3) and (D4) shown as dashed lines with the numerical dispersion relations plotted as dots obtained by integrating equations (20)–(23) subject to the rigid BCs. An isothermal disk with $A = 0.8$ and $\kappa_0^2/(2\pi G\rho_{00}) = 0.2$ is considered for the numerical calculations using the method described in Appendix C. Only the results for the fundamental acoustic modes (i.e., no node in the z-direction) and the lowest-order inertial modes with a single node are shown. The inset in Figure 12b enlarges the regions with $0.7 \le k_x H \le 0.8$ and $0.15 \le \omega^2/(2\pi G\rho_{00}) \le 0.21$, where the acoustic and inertial modes cross each other. In plotting equations (D3) and (D4), we utilize the eigenfunctions and their derivatives at $z = 0$ to calculate β and k_z. Note that agreement between the local and numerical dispersion relations is excellent for the non-self-gravitating case. Self-gravity makes $\beta \lesssim -0.4$ for the acoustic modes, making them unstable for $0.12 < k_x H < 0.63$. On the other hand, the inertial modes have $\beta c_s^2 k_z^2/\kappa_0^2 \gtrsim 38$ and thus remain stable even in the presence of self-gravity.

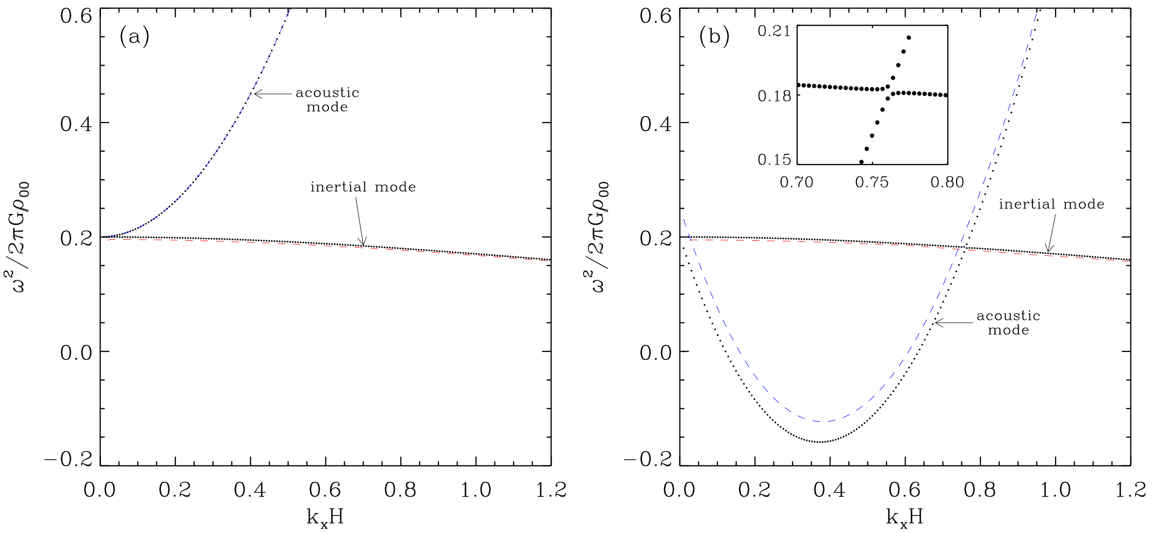

Figure 12. Comparison of the local dispersion relations (dashed lines) with the numerical dispersion relations (dots) for acoustic and inertial modes in (a) non-self-gravitating and (b) self-gravitating cases. For the numerical results, an isothermal disk with $A = 0.8$ and $\kappa_0^2/(2\pi G\rho_{00}) = 0.2$ is taken and the rigid BCs are adopted. In (a), the local dispersion relations are almost identical to the numerical results. In (b), the acoustic and inertial modes cross each other near $k_xH = 0.77$, and the inset zooms in on the crossing regions. While self-gravity changes the acoustic mode dramatically, the inertial modes are almost intact.

As in our present work, Mamatsashvili & Rice (2010) also calculated dispersion relations of waves in vertically-stratified, polytropic, rotating disks. Except for the internal gravity waves arising from convective motions that are missing in our models, their numerical results are qualitatively similar to ours.[2] In interpreting their results, however, they argued that the influence of self-gravity is strongest on the inertial mode and that GI results from the first harmonics of the inertial mode. This erroneous finding seemingly results from the observation that the long-wavelength unstable branch of the dispersion curves are smoothly connected to the short-wavelength part of the inertial modes, which occurs at $k_xH \simeq 0.77$ in Figure 12b. They claimed that the frequency ordering $\omega_r^2 \leq \kappa_0^2 < \omega_p^2$ which is valid in the non-self-gravitating case holds true also for the the self-gravitating counterpart, so that the lowest-frequency modes are always the inertial modes regardless of k_x. However, our local dispersion relations (eqs. (D3) and (D4)) show that this is correct only when $\beta > 0$, i.e., only for waves with relatively short wavelength.[3] For gravitationally unstable modes with $\beta < -\kappa_0^2/(c_s^2k^2)$, $\omega_p^2 < 0 < \omega_r^2 \leq \kappa_0^2$. In Figure 12b, the lower-frequency mode at $k_xH < 0.77$ is connected to the higher-frequency acoustic mode at $k_xH > 0.77$, while the higher-frequency mode at $k_xH < 0.77$ is connected to the lower-frequency inertial mode at $k_xH > 0.77$. When the inertial and acoustic modes are mixed together by having similar frequencies and wavenumbers, it is quite ambiguous to tell which one is which near $k_xH = 0.77$.

D.2. *Comparison of Eigenfunctions*

A clear way to distinguish the modes is to compare the corresponding eigenfunctions since they contain information on mode characteristics. Inertial modes, being incompressible in nature, should involve very weak density perturbations. This can be readily seen from equation (D2) since

$$\frac{|\rho_1/\rho_0|}{|u_{1x}/c_s|} = \frac{|\omega^2 - \kappa_0^2|}{|\beta\omega|c_sk_x} \approx \frac{\kappa_0 k_x}{\beta c_s k_z^2} \ll 1, \tag{D5}$$

for inertial modes with $k_x/k_z \ll 1$. On the other hand, acoustic modes with $k_x/k_z \gg 1$ have $|\rho_1/\rho_0|/|u_{1x}/c_s| \approx c_sk_x/|\omega_p| \sim O(1)$, implying that they rely on relatively large density perturbations.

Figure 13 plots the vertical profiles of the numerically-calculated eigenfunctions u_{1x}, u_{1z}, and ρ_1/ρ_0 of the fundamental acoustic modes (left panels) and the lowest-order inertial modes (right panels). The background state is the same as in Figure 12. The most-unstable wavenumber $k_xH = 0.37$, well away from $k_xH = 0.77$ where the two modes are mixed, is chosen for all modes. The solid and dashed lines correspond to the cases with and without self-gravity, respectively. The normalization is such that $u_{1x}/c_s = 1$ at $z = 0$. The non-self-gravitating acoustic mode has $\omega^2/(2\pi G\rho_{00}) = 0.41$, $k_z = 0$, $u_{1x}/c_s = 1$, $u_{1z} = 0$, and $\rho_1/\rho_0 = 0.57$, independent of z, which are in fact exact solutions (see Appendix E). When self-gravity is included, the acoustic mode becomes unstable with $\omega^2/(2\pi G\rho_{00}) = -0.16$; the corresponding eigenfunctions varies with z only sightly with $k_zH = 0.11$, but they do not have any node. For

---

[2] Note that Mamatsashvili & Rice (2010) considered disks with $\gamma > 1$ and $p_{\rm ext} = 0$, automatically truncated at $z = z_{\rm cut}$ (see eq. [13]). With the imposed free BCs, they identified surface-gravity waves (f mode), although the destabilizing effect of surface distortion is absent in their models.

[3] This is usually the case in stellar interiors since $c_s^2 \sim \pi G\rho_0 R^2$ from the condition of hydrostatic equilibrium, with R denoting the stellar radius. Then, $\beta \simeq 1 - 0.1(\lambda/R)^2 > 0$ for waves with wavelength $\lambda < R$.

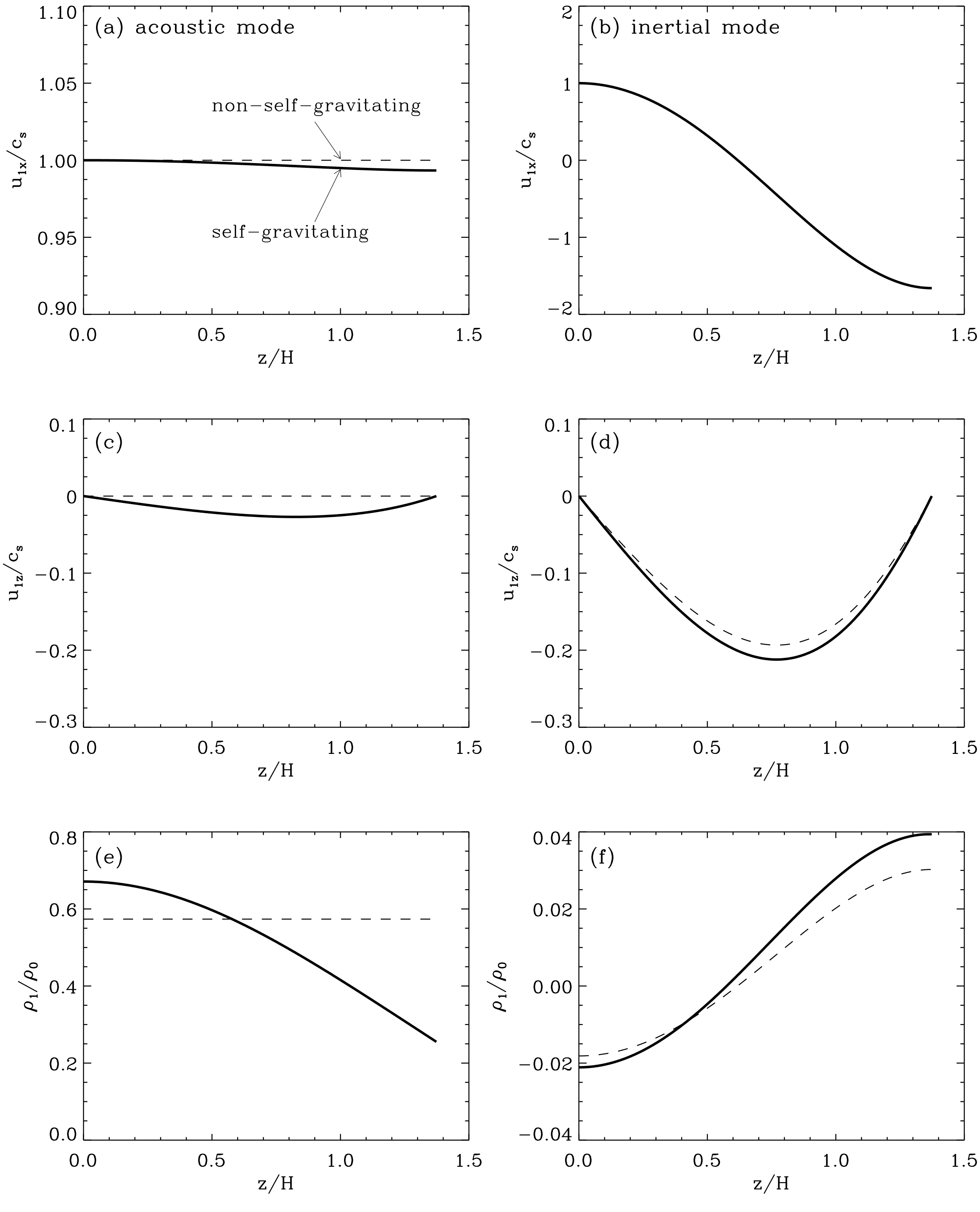

Figure 13. Comparisons of the eigenfunctions for the acoustic modes (left panels) and the lowest-order inertial modes (right panels) with $k_xH = 0.37$ shown in Figure 12. The solid and dashed lines correspond to the self-gravitating and non-self-gravitating modes, respectively. All eigenfunctions are normalized such that $u_{1x} = 1$ at $z = 0$. Note that the inertial modes involve very little density perturbations and are almost unaffected by self-gravity, while the acoustic modes have $|u_{1z}/u_{1x}| \ll 1$ since they propagate primarily along the horizontal direction.

acoustic modes, $|u_{1z}/u_{1x}| \ll 1$ for $k_z/k_x \ll 1$, consistent with the prediction of the local analysis. The amplitude of the perturbed density for the acoustic modes is of order unity relative to the velocity perturbations. On the other hand, the inertial modes have a node at around $z/H \sim 0.57$–0.61, regardless of the presence of self-gravity. Gravity makes little change in u_{1x} and small changes in u_{1z} and ρ_1. The corresponding eigenfrequencies and vertical wavenumbers are $\omega^2/(2\pi G\rho_{00}) = 0.1954, 0.1949$ and $k_zH = 2.424, 2.421$ in non-self-gravitating and self-gravitating cases, respectively. Note that $|\rho_1/\rho_0|/|u_{1x}/c_s| \ll 1$ for the inertial modes, just as expected.

All of the above results suggest that the acoustic modes are strongly affected by self-gravity to be unstable when self-gravity is sufficiently strong, and that the inertial modes are not much influenced by self-gravity and remain stable.

E. SOLUTIONS FOR WAVES IN NON-SELF-GRAVITATING DISKS

When $\psi_1 = \kappa_0 = 0$, equations (20) and (21) become

$$\frac{d\xi_{1z}}{dz} = \frac{k^2}{\omega^2}h_1 - \frac{1}{c_s^2}(h_1 - g_0\xi_{1z}), \tag{E1}$$

$$\frac{dh_1}{dz} = \omega^2\xi_{1z}. \tag{E2}$$

In equation (E1), the vertical gravity g_0 should be considered as being external. Substituting equation (E2) into equation (E1), we obtain

$$\frac{d}{dz}\left(\rho_0\frac{d}{dz}h_1\right) + \left(\frac{\omega^2}{c_s^2} - k_x^2\right)\rho_0 h_1 = 0, \tag{E3}$$

where the equilibrium condition $d\rho_0/dz = -g_0\rho_0/c_s^2$ is used. Note that equation (E3) together with the rigid BCs and the symmetry constraint at the midplane is in the Sturm-Liouville form with eigenvalue

$$k_z^2 \equiv \omega^2/c_s^2 - k_x^2, \tag{E4}$$

indicating that the fundamental modes have the lowest frequency (thus most susceptible to GI).

For a time being, we limit to an isothermal disk with $\rho_0 \propto \mathrm{sech}^2(z/H_0)$ for which analytic solutions of equation (E3) can be derived. In terms of the dimensionless variable μ (eq. [A11]), equation (E3) becomes

$$(1-\mu^2)\frac{d^2v}{d\mu^2} - 2\mu\frac{dv}{d\mu} + \left(2 - \frac{\lambda^2}{1-\mu^2}\right)v = 0\,, \tag{E5}$$

where $v \equiv (1-\mu^2)^{1/2}h_1$ and $\lambda^2 = 1 - (k_zH_0)^2$. The above equation is of the associated Legendre type whose solution is given by

$$v = C_1P_1^{\lambda} + C_2P_1^{-\lambda}, \tag{E6}$$

where C_1 and C_2 are constants to be determined, and $P_1^{\pm\lambda}$ is the Ferrers' associated Legendre function defined as

$$P_1^{\pm\lambda} = (\lambda \mp \mu)\left(\frac{1+\mu}{1-\mu}\right)^{\pm\lambda/2}, \tag{E7}$$

(Whittaker & Watson 1963).

The even-symmetry condition, $dv/d\mu|_{\mu=0}$, at the midplane requires $C_1 = C_2$. After some manipulations, we find h_1 in terms of z as

$$h_1 = \sinh(z/H_0)\sin(\widetilde{k_z}z) - \widetilde{k_z}H_0\cosh(z/H_0)\cos(\widetilde{k_z}z), \tag{E8}$$

where $\widetilde{k_z} \equiv \sqrt{k_z^2 - H_0^{-2}}$ and the proportionality constant C_1 or C_2 is omitted. The vertical wavenumber that satisfies the rigid BC, $dh_1/dz|_{z=a} = 0$, is then given by

$$k_{z,n}^2 = \begin{cases} 0, & \text{for fundamental mode,} \\ n^2\pi^2/a^2 + 1/H_0^2, & \text{for harmonics with order } n = 1, 2, 3, \cdots. \end{cases} \tag{E9}$$

Now we consider general polytropic disks, and seek for fundamental-mode solutions of (E3). While equation (E3) cannot be solved in a closed form for arbitrary γ, it has the simplest but important solution

$$h_1 \to \text{constant}, \tag{E10}$$

in the long-wavelength limit regardless of the BCs. This corresponds to equation (E8) with $k_z = 0$ for isothermal disks. For waves with $k_xH \ll 1$, gas motions are restricted mostly to the horizontal direction. In this case, the acceleration of the gas along the vertical direction ($-\omega^2\xi_{1z}$ in eq. [E2]) becomes relatively unimportant, resulting in $dh_1/dz \approx 0$. As Figure 2 shows, $h_1 \approx$ constant is reasonably good for $k_xH \lesssim 1$.

Another limiting case is a strongly confined disk with $A \ll 1$, for which $\rho_0(z) =$ constant and $\omega^2/c_s^2 \ll k_x^2$, the latter of which shall be verified a posteriori. Then, the even-symmetry solution of equation (E3) is

$$h_1 \propto \cosh(k_xz), \tag{E11}$$

which corresponds to equation (E8) in the limit of $\widetilde{k_z} \to ik_x$ and $z/H_0 \ll 1$. In this case, $\nabla\cdot\boldsymbol{\xi_1} = 0$ and the system is essentially incompressible. Note that equation (34) gives $\omega^2/c_s^2 < (g_{0a}H/c_s^2)k_x^2 \ll k_x^2$, as expected.

Up to now we have ignored the effect of disk rotation, but it is a simple matter to show that the above results are valid also for rotating disks provided k_z in equation (E4) is changed to

$$k_z^2 = \frac{\omega^2}{c_s^2} - \frac{\omega^2}{\omega^2 - \kappa_0^2} k_x^2 \,, \tag{E12}$$

which is identical to equation (D1). This implies that the local solutions presented in Appendix D are exact for non-self-gravitating, isothermal disks.

REFERENCES

Abramowitz, M., & Stegun, I. A. 1972, Handbook of Mathematical Functions
Bell, K. R., Cassen, P. M., Klahr, H. H., & Henning, T. 1997, ApJ, 486, 372
Binney, J., & Tremaine, S. 2008, Galactic Dynamics: Second Edition (Princeton University Press)
Boley, A. C., Durisen, R. H., Nordlund, Å., & Lord, J. 2007, ApJ, 665, 1254
Boley, A. C., Mejía, A. C., Durisen, R. H., Cai, K., Pickett, M. K., & D'Alessio, P. 2006, ApJ, 651, 517
Boss, A. P. 1997, Science, 276, 1836
Boyd, D. F. A., & Whitworth, A. P. 2005, A&A, 430, 1059
Chandrasekhar, S. 1961, Hydrodynamic and hydromagnetic stability
Churchwell, E., et al. 2006, ApJ, 649, 759
—. 2007, ApJ, 670, 428
Dale, J. E., Wünsch, R., Smith, R. J., Whitworth, A., & Palouš, J. 2011, MNRAS, 411, 2230
Dale, J. E., Wünsch, R., Whitworth, A., & Palouš, J. 2009, MNRAS, 398, 1537
D'Alessio, P., Canto, J., Calvet, N., & Lizano, S. 1998, ApJ, 500, 411
Deharveng, L., Zavagno, A., & Caplan, J. 2005, A&A, 433, 565
Dubois, Y., & Teyssier, R. 2008, A&A, 477, 79
Durisen, R. H., Boss, A. P., Mayer, L., Nelson, A. F., Quinn, T., & Rice, W. K. M. 2007, Protostars and Planets V, 607
Elmegreen, B. G. 1982, ApJ, 253, 634
—. 1987, ApJ, 312, 626
—. 1989, ApJ, 340, 786
Elmegreen, B. G. 1998, in Astronomical Society of the Pacific Conference Series, Vol. 148, Origins, ed. C. E. Woodward, J. M. Shull, & H. A. Thronson Jr., 150
Elmegreen, B. G., & Elmegreen, D. M. 1978, ApJ, 220, 1051
Elmegreen, B. G., & Lada, C. J. 1977, ApJ, 214, 725
Goldreich, P., & Lynden-Bell, D. 1965a, MNRAS, 130, 97
—. 1965b, MNRAS, 130, 125
Goldreich, P., & Tremaine, S. 1978, ApJ, 222, 850
Harrison, E. R., & Lake, R. G. 1972, ApJ, 171, 323
Hosokawa, T., & Inutsuka, S.-i. 2006, ApJ, 646, 240
Iwasaki, K., Inutsuka, S.-i., & Tsuribe, T. 2011, ApJ, 733, 16
Julian, W. H., & Toomre, A. 1966, ApJ, 146, 810
Kim, W.-T., Ostriker, E. C., & Stone, J. M. 2002, ApJ, 581, 1080
Kim, W.-T., & Ostriker, E. C. 2007, ApJ, 660, 1232
Kim, W.-T., Ostriker, E. C., & Stone, J. M. 2003, ApJ, 599, 1157
Korycansky, D. G., & Pringle, J. E. 1995, MNRAS, 272, 618
La Dous, C. 1994, Space Sci. Rev., 67, 1
Larson, R. B. 1985, MNRAS, 214, 379
Latter, H. N., & Balbus, S. A. 2009, MNRAS, 399, 1058
Ledoux, P. 1951, Annales d'Astrophysique, 14, 438
Lee, S. M., & Hong, S. S. 2007, ApJS, 169, 269
Lighthill, J. 1978, Waves in fluids (Cambridge University Press)
Lin, D. N. C., Papaloizou, J. C. B., & Savonije, G. J. 1990, ApJ, 364, 326
Lubow, S. H., & Ogilvie, G. I. 1998, ApJ, 504, 983
Lubow, S. H., & Pringle, J. E. 1993, MNRAS, 263, 701
Mamatsashvili, G. R., & Rice, W. K. M. 2010, MNRAS, 406, 2050
McKee, C. F., & Ostriker, E. C. 2007, ARA&A, 45, 565
Mejía, A. C., Durisen, R. H., Pickett, M. K., & Cai, K. 2005, ApJ, 619, 1098
Nagai, T., Inutsuka, S.-I., & Miyama, S. M. 1998, ApJ, 506, 306
Nelson, A. F., Benz, W., & Ruzmaikina, T. V. 2000, ApJ, 529, 357
Ogilvie, G. I., & Lubow, S. H. 1999, ApJ, 515, 767
Rice, W. K. M., Armitage, P. J., Bate, M. R., & Bonnell, I. A. 2003, MNRAS, 339, 1025
Rice, W. K. M., Lodato, G., & Armitage, P. J. 2005, MNRAS, 364, L56
Safronov, V. S. 1960, Annales d'Astrophysique, 23, 979
Simon, R. 1965, Annales d'Astrophysique, 28, 40
Toomre, A. 1964, ApJ, 139, 1217
Umekawa, M., Matsumoto, R., Miyaji, S., & Yoshida, T. 1999, PASJ, 51, 625
Usami, M., Hanawa, T., & Fujimoto, M. 1995, PASJ, 47, 271
Viala, Y., & Horedt, G. P. 1974, A&AS, 16, 173
Voit, G. M. 1988, ApJ, 331, 343
Whittaker, E. T., & Watson, G. N. 1963, A course of modern analysis
Wünsch, R., Dale, J. E., Palouš, J., & Whitworth, A. P. 2010, MNRAS, 407, 1963
Wünsch, R., Jáchym, P., Sidorin, V., Ehlerová, S., Palouš, J., Dale, J., Dawson, J. R., & Fukui, Y. 2012, A&A, 539, A116
Zapatero Osorio, M. R., Béjar, V. J. S., Martín, E. L., Rebolo, R., Barrado y Navascués, D., Mundt, R., Eislöffel, J., & Caballero, J. A. 2002, ApJ, 578, 536
Zel'Dovich, Y. B. 1970, A&A, 5, 84